

Composite Fermi Liquid at Zero Magnetic Field in Twisted MoTe₂

Junkai Dong,^{1,*} Jie Wang,^{1,2,†} Patrick J. Ledwith,^{1,‡} Ashvin Vishwanath,^{1,§} and Daniel E. Parker^{1,¶}

¹*Department of Physics, Harvard University, Cambridge, MA 02138, USA*

²*Center for Mathematical Sciences and Applications,
Harvard University, Cambridge, MA 02138, USA*

The pursuit of exotic phases of matter outside of the extreme conditions of a quantizing magnetic field has been a long standing quest of solid state physics. Recent experiments have observed spontaneous valley polarization and fractional Chern insulators (FCIs) in zero magnetic field in twisted bilayers of MoTe₂, at partial filling of the topological valence band ($\nu = -2/3$ and $-3/5$). We study the topological valence band at *half* filling, using exact diagonalization and density matrix renormalization group calculations. We discover a composite Fermi liquid (CFL) phase even at zero magnetic field that covers a large portion of the phase diagram centered around twist angle $\sim 3.6^\circ$. The CFL is a non-Fermi liquid phase that shows metallic behavior despite the absence of Landau quasiparticles. We discuss experimental implications including the competition between the CFL and a Fermi liquid, which can be tuned with a displacement field. The topological valence band has excellent quantum geometry over a wide range of twist angles and a small bandwidth that is, remarkably, reduced by interactions for a range of angles. These key properties are responsible for stabilizing the exotic quantum Hall phases we find at zero field. Finally, we present an optical signature involving “extinguished” optical responses as a means to identify Chern bands with ideal quantum geometry.

Introduction.—Strong interactions can lead to exotic phases of matter such as non-Fermi-liquids. A remarkable example is the composite Fermi liquid (CFL) that occurs in a half or quarter filled lowest Landau level (LLL). The CFL is a non-Fermi liquid with an emergent Fermi sea composed of charge neutral “composite fermions” [1–4] and has anomalous responses to a wide variety of experimental probes [5–10]. The gapless CFL state is regarded as the “parent state” for various types of Abelian [1–4] and non-Abelian gapped topological phases [11].

In this work, we propose an alternative route for realizing CFLs. Our proposal is based on twisted 2D transition metal dichalcogenides (TMD), a family of platforms that have realized a wealth of interesting phenomena [12–27] and generated much theoretical interest for their topological properties [28–41]. Recent experiments [26, 27] have provided strong evidence for zero field fractional Chern insulators (FCI) [42–45] at fillings $\nu = -2/3$ and $-3/5$ in twisted bilayers of MoTe₂, following theoretical work, in particular [29], which argued for Chern bands in twisted homo-bilayers of TMDs such as MoTe₂. The possibility of FCIs on partially filling these bands was discussed previously in MoTe₂ [46] and in WSe₂ [47, 48]. Theoretical studies combining ab-initio and numerical exact diagonalization methods of the MoTe₂ [49, 50] have also obtained FCIs, despite somewhat different ab-initio models.

FCIs were previously reported at high magnetic fields

[51] by partially filling Hofstadter bands [52] of a substrate induced moiré potential in graphene. Shortly thereafter, with the discovery of correlated phenomena [53, 54] and spontaneous Chern insulators [55, 56] in twisted bilayer graphene (TBG), fractional Chern insulators in zero field were theoretically anticipated in magic-angle TBG [57–59]. Experimental observation of FCIs in this setting soon followed, albeit with the assistance of a small magnetic field [60] which was addressed in subsequent theory in terms of the field-induced improvement of the quantum geometry and dispersion of TBG [61]. Here we will see that twisted MoTe₂ circumvents some of the challenges posed by TBG in realizing zero-field FCIs.

We focus on the gapless CFL phase, which presents challenges [62] relative to the well-understood spectral and entanglement signatures [63] present in gapped FCI phases. Using combined large scale exact diagonalization (ED) and density matrix renormalization group (DMRG) methods, we show that the CFL phase can be realized in a large portion of the parameter space of moiré MoTe₂. We outline a conceptual framework to describe zero field CFLs with an explicit trial wavefunction that captures the essential features of the state and its low energy spectrum. Finally, we discuss experimental signatures that would experimentally contrast the CFL phase from the Fermi liquid and aid in its experimental detection.

Continuum model.—We consider a standard model [29] for holes in the valence bands of a twisted TMD with gate-screened Coulomb interactions

$$\hat{H} = -\hat{h} + \frac{1}{2A} \sum_{\mathbf{q}} V_{\mathbf{q}} : \hat{\rho}_{\mathbf{q}} \hat{\rho}_{-\mathbf{q}} :, \quad V_{\mathbf{q}} = \frac{2\pi \tanh(qd)}{\epsilon_r \epsilon_0 q}, \quad (1)$$

where $\hat{\rho}_{\mathbf{q}}$ is the density operator, A is the sample area, normal ordering is relative to filling $\nu = 0$, and $\epsilon_r \approx 5-15$ is the dielectric constant. The kinetic Hamiltonian in

* junkaidong@g.harvard.edu

† jiewang@fas.harvard.edu

‡ pledwith@g.harvard.edu

§ avishwanath@g.harvard.edu

¶ daniel_parker@fas.harvard.edu

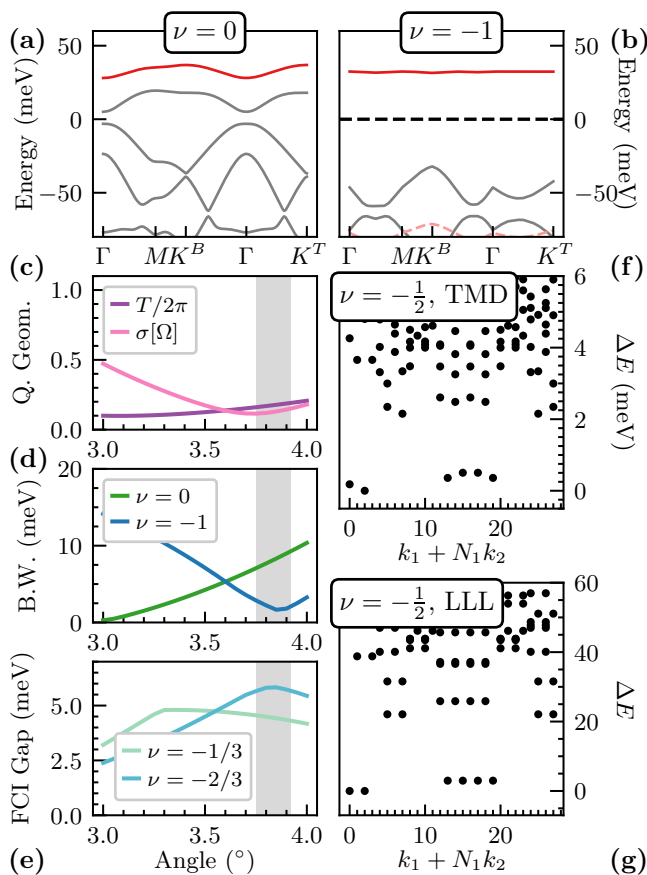


FIG. 1. The top valence band has favorable conditions for fractionalized topological phases. Bandstructure as seen from (a) charge neutrality and (b) from $\nu = -1$ computed from self-consistent Hartree-Fock. At $\nu = -1$ interactions reduce the bandwidth five-fold from 9 meV to 1.8 meV. (c) Quantum geometry in terms of trace condition T and Berry curvature deviation $\sigma[\Omega]$. The trace condition is nearly satisfied, and the Berry curvature is almost flat. (d) Bare and SCHF bandwidths and (e) the many-body gap of FCIs at $\nu = -1/3$ and $\nu = -2/3$ as a function of twist angle. The FCI gaps are obtained from ED with $N_e = 8$ and 16 respectively. The SCHF bandwidth reaches a minimum around 3.9° , in excellent agreement with the peak of the FCI gap at $\nu = -2/3$. (f) and (g): ED spectrum for 14 particles at half filling for Coulomb interaction in lowest Landau level and screened Coulomb interaction in twisted MoTe₂, respectively. The close correspondence of the low energy spectrum states confirms that the ground state in MoTe₂ is a CFL. Parameters: $(\theta, \epsilon_r, d) = (3.89^\circ, 8, 300 \text{ \AA})$ unless otherwise noted.

valley K is [29]:

$$h_K = \begin{bmatrix} h^b(\mathbf{r}) + V/2 & T(\mathbf{r}) \\ T^\dagger(\mathbf{r}) & h^t(\mathbf{r}) - V/2 \end{bmatrix} \quad (2)$$

where $h^\ell(\mathbf{r}) = -(\mathbf{p} - \hbar v_F \mathbf{K}^\ell)^2 / 2m^* + \Delta^\ell(\mathbf{r})$. Here the layer-diagonal terms include the quadratic monolayer TMD dispersion centered at rotated monolayer K -points $\mathbf{K}^{t/b}$, shifted by the displacement field V , and the moiré potentials $\Delta^{b/t}(\mathbf{r}) = 2v \sum_{j=1,3,5} \cos(\mathbf{b}_j \cdot \mathbf{r} \pm \psi)$.

The off-diagonal terms correspond to the interlayer tunneling $T(\mathbf{r}) = \omega(1 + e^{i\mathbf{b}_2 \cdot \mathbf{r}} + e^{i\mathbf{b}_3 \cdot \mathbf{r}})$, where \mathbf{b}_j are the reciprocal vectors obtained by counterclockwise $(j-1)\pi/3$ rotations of $\mathbf{b}_1 = (4\pi 3^{-1/2}\theta/a_0, 0)$. Due to the strong intrinsic spin-valley locking of TMDs, the low energy holes of the K valley are locked to spin up. Time-reversal symmetry determines the other spin-valley locked component $h_{K'}$. The full kinetic term is $\hat{h} = h_K + h_{K'}$. We focus on MoTe₂, where recent first-principles calculations [49] found $(a_0, m^*, V, \psi, \omega) = (3.52 \text{ \AA}, 0.6m_e, 20.8 \text{ meV}, -107.7^\circ, -23.8 \text{ meV})$ at $\theta = 3.89^\circ$ (see also [29, 50]).

Flat Almost-Ideal Chern Band.—Fig. 1(a) shows the bandstructure for holes $-h_K$. The top moiré band has Chern number $C = 1$, due to the skyrmionic character of the layer spinor [29], and has a small bandwidth of ~ 9 meV.

Recent experiments [26, 27] demonstrate that the many-body ground state is ferromagnetic (valley-polarized) in at least the range $-1.2 \lesssim \nu \lesssim -0.4$. The “parent state” for this regime is the correlated insulating state at $\nu = -1$. Fig. 1(b) shows its bandstructure within self-consistent Hartree-Fock (SCHF), which is strongly renormalized by interactions. Strikingly, the renormalized $C = 1$ band (red) becomes almost exactly flat, with bandwidth 1.8 meV at $\theta = 3.89^\circ$. This *reduction* [64] in bandwidth from interaction effects is highly unusual [65].

For such bands with narrow dispersion relative to the interaction scale, the many-body ground state is determined by the character of single particle wavefunctions of the band. Recent theories point out the importance of momentum space Kähler geometry to the stability of FCIs [42, 57, 66–77]. We say that a band has “ideal quantum geometry” if the trace inequality $T = \int d^2\mathbf{k} (\text{Tr } g_{\text{FS}}(\mathbf{k}) - \Omega(\mathbf{k})) \geq 0$ is saturated [57, 69, 73, 78]; here g_{FS} is the Fubini-Study metric and Ω is the Berry curvature. Ideal bands are “vortexable” in the sense that $zP = PzP$ where P is the projector onto the band and $z = x + iy$ is a vortex function [75, 79]. We use “vortexability” and “ideal quantum geometry” interchangeably. Vortexability enables the direct construction of Laughlin-like FQHE trial states that are exact many-body ground states for ideal bands with short-range interactions [75, 79, 80]. Fig. 1(c) shows the quantity T , the deviation from ideality, and $\sigma[\Omega]$, the standard deviation of Berry curvature. Both are small in twisted MoTe₂ for $3^\circ \leq \theta \leq 4^\circ$. The top valence band thus has the rare combination of excellent quantum geometry and negligible bandwidth that favors lattice realizations of exotic quantum Hall states at zero magnetic field.

The interacting physics of the top valence band is modeled by projecting Eq. (1) via $-\hat{h} \rightarrow \sum_{\mathbf{k}} \epsilon(\mathbf{k}) \hat{c}_{\mathbf{k}}^\dagger \hat{c}_{\mathbf{k}}$ and $\hat{\rho}_{\mathbf{q}} \rightarrow \bar{\rho}_{\mathbf{q}} = \sum_{\mathbf{k}} \hat{c}_{\mathbf{k}}^\dagger \langle u_{\mathbf{k}} | u_{\mathbf{k}+\mathbf{q}} \rangle \hat{c}_{\mathbf{k}+\mathbf{q}}$ where $\epsilon(\mathbf{k})$ and $u_{\mathbf{k}}$ are the dispersion and periodic part of Bloch wavefunction, respectively. As large bandwidths destabilize FCIs in favor of metallic states, we focus on angles $3-4^\circ$. Fig. 1(d) shows the bare ($\nu = 0$) and renormalized ($\nu = -1$) bandwidths as a function of twist angle, showing minima near

3° and 3.89°, respectively. Fig. 1(e) confirms that fractional Chern insulators are stabilized at $\nu = -1/3, -2/3$ — in concord with previous results [46, 49, 50]. Notably the gap at $\nu = -2/3$ is largest where the bandwidth at $\nu = -1$ is smallest (gray region), while the $\nu = -1/3$ gap is maximized at a smaller angle $\sim 3.3^\circ$. We therefore expect in-between angles, around 3.6° , to be optimal for FQH physics near $\nu = -1/2$ for our choice of microscopic parameters.

Composite Fermi liquid at $\nu = -1/2$. — We now move beyond gapped FCIs and focus on more exotic gapless CFL states occurring at even denominator fillings, which are “parent states” for gapped FCIs [1, 11]. We mainly focus on $\nu = -1/2$ but also discuss $\nu = -3/4$, a filling fraction closer to the optimal band limit $\nu = -1$ at twist angle 3.89° . We now present strong evidence for the CFL phase from both ED and DMRG.

(i) *Many body spectrum:* Fig. 1(f, g) compares the spectra of twisted MoTe₂ and the lowest Landau level (LLL) at half filling with 14 electrons, showing a one-to-one correspondence at low energy. The LLL spectrum uses the same geometry as moiré MoTe₂ with Coulomb interactions. This one-to-one similarity holds at all system sizes $N_e = 8 - 14$. We thus conclude that the ground state of \hat{H} at $\nu = -1/2$ is the same phase as the half-filled LLL with Coulomb interactions — the CFL. The ground state and low-energy excitations are at precisely the momenta expected for compact composite Fermi sea (CFS) configurations [81]. See SM for other system sizes and detailed matching of degeneracies, momenta, and excitations to CFL expectations.

(ii) *Absence of electron Fermi surface:* A finite quasi-particle weight $Z > 0$ gives the jump in electron occupations $n(\mathbf{k})$ at the Fermi surface in a regular Fermi liquid (FL). As a non-Fermi liquid, composite fermions have vanishing Z , leading to absence of a jump and uniform $n(\mathbf{k}) \approx \nu$.

To characterize the emergent composite Fermi liquid we employ large-scale iDMRG calculations. We use an infinite cylinder geometry with circumference $L_y = 5 - 10$, corresponding to L_y evenly spaced horizontal wires through the Brillouin zone (Fig. 2(c) inset). We take a computational basis of hybrid Wannier-Qi orbitals [82], and use “MPO compression” [83, 84] to accurately capture gate-screened Coulomb interactions ($d = 100 \text{ \AA}$) in the flat band. Under weak interactions ($\epsilon_r = 60$), we find the Fermi liquid expected from band theory at $\nu = -1/2$, with an almost-circular Fermi surface centered at Γ (Fig. 2(a), left) with radius $k_F = (A_{BZ}/2\pi)^{1/2}$. As electrons, holes, and particle-hole pairs are gapless in a FL, one expects DMRG correlation lengths to diverge with bond dimension for electric charge $Q_E = 0, \pm 1$ sectors — which we observe (see SM).

Under realistic interactions ($\epsilon_r = 6$) with the same parameters, the ground state has uniform occupations $|n(\mathbf{k}) - \frac{1}{2}| < 0.05$ (Fig. 2(a), right) and rapidly decaying single electron correlation function. Although electron correlations are strong, they do not manifest in $Q_E = 1$

correlations, which decay rapidly, inconsistent with an electron-like Fermi surface. However, the state has high entanglement and significant electrically neutral correlations, consistent with the gapless density fluctuations expected from an emergent CFS. To reveal the “hidden” CFS, we turn to the structure factor.

(iii) *Scattering across the composite Fermi sea:* Fig. 2(b) contrasts the connected structure factor $S(\mathbf{q}) = \langle \hat{\rho}_{\mathbf{q}} \hat{\rho}_{-\mathbf{q}} \rangle - \langle \hat{\rho}_{\mathbf{q}} \rangle \langle \hat{\rho}_{-\mathbf{q}} \rangle$ between the Fermi liquid and the composite Fermi liquid. Both correlation functions nearly vanish when $|\mathbf{q}| > 2k_F$, where $k_F = (A_{BZ}/2\pi)^{1/2}$, strongly implying that there is a Fermi surface in the CFL phase where the constituent fermions aren’t electrons. We then match the non-analyticities of $S(\mathbf{q})$ to scattering events with different momentum transfers across the putative CFS in Fig. 2(c), e.g. $\hat{c}_{\mathbf{k}=G}^\dagger \hat{c}_{\mathbf{k}=B}$ scattering with $q_x \approx 1.94k_F$. The *tour-de-force* work of Geraedts *et al* [62] showed such features are emblematic of the CFS arising from the half-filled LLL. As every feature in $S(\mathbf{q})$ corresponds to such a scattering (quantitative matching in SM), we conclude the state has an almost-circular [85] CFS composed of non-Landau quasiparticles. Based on these two independent numerical methods, we have determined the presence of a CFL phase at $\nu = -1/2$ (see SM for $\nu = -3/4$).

Zero Field CFL Wavefunction and parton theory. — In this section, we discuss how composite fermions in Chern bands can directly relate to those of the LLL, despite the absence of real magnetic flux. To do so, we construct an explicit zero-field CFL wavefunction and interpret it through a parton theory [86–91]

Our construction will be motivated by the TMD wavefunctions in the vortexable limit. The wavefunctions of $C = 1$ ideal bands have the general “LLL-like” form [57, 73],

$$\psi_l(\mathbf{r}) = f(z)e^{-K(\mathbf{r})}\zeta_l(\mathbf{r}) \quad (3)$$

where $f(z)$ is any holomorphic function and $\zeta_l(\mathbf{r})$ is an orbital-space spinor that satisfies $\sum_l |\zeta_l(\mathbf{r})|^2 = 1$. The first two terms, $\phi(\mathbf{r}) = f(z)e^{-K(\mathbf{r})}$, may be interpreted as the wavefunction of a Dirac particle in an inhomogeneous, periodic, magnetic field $B(\mathbf{r}) = \nabla^2 \text{Re}K(\mathbf{r})$ with one flux quantum per unit cell [57, 92, 93]. Note that while ψ is symmetric under ordinary translations, $\phi(\mathbf{r})$ and $\zeta_l(\mathbf{r})$ are symmetric under *magnetic* translations, with opposite magnetic twists [94], and there is a gauge redundancy under which $\phi(\mathbf{r}) \rightarrow e^{+i\lambda(\mathbf{r})}\phi(\mathbf{r})$ and $\zeta_l(\mathbf{r}) \rightarrow e^{-i\lambda(\mathbf{r})}\zeta_l(\mathbf{r})$.

Motivated by near-ideal geometry, and the form of the idealized band wavefunctions (3), we may construct an ansatz for the N -electron CFL wavefunction based on the Read and Rezayi LLL ansatz [95]:

$$\Psi(\{\mathbf{r}_i\}) = \mathcal{P} \det_{ij} \psi_{\mathbf{k}_i}^{\text{CF}}(\mathbf{r}_j) \prod_{i < j} (z_i - z_j)^2 \prod_i e^{-K(\mathbf{r}_i)} \zeta_{l_i}(\mathbf{r}_i) \quad (4)$$

Here $\mathcal{P} = \prod_i P_i$ is the many-body projector onto the band of interest, $\psi_{\mathbf{k}}^{\text{CF}}(\mathbf{r})$ is a Bloch wavefunction of a

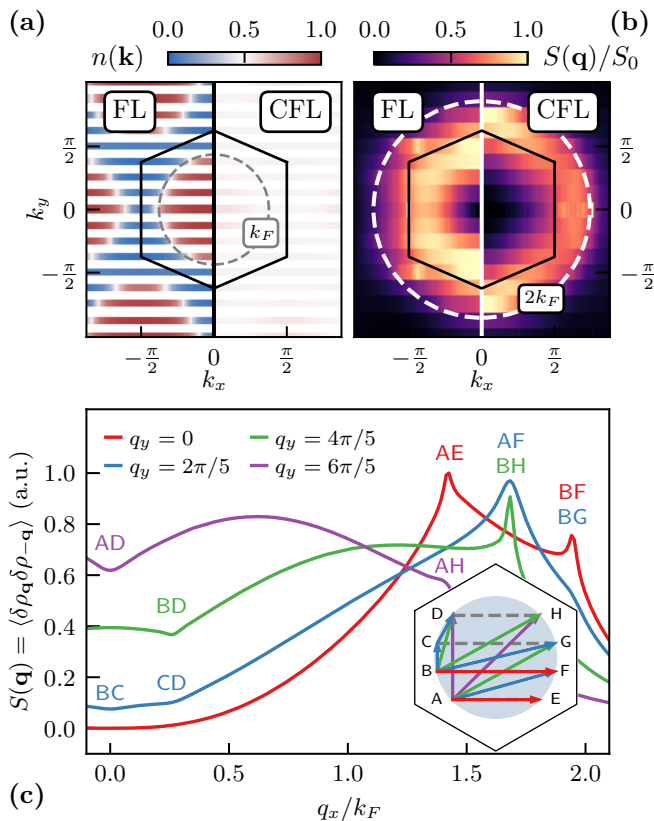


FIG. 2. Numerical identification of the composite Fermi liquid (CFL) from iDMRG. (a) Occupations $n(\mathbf{k})$ in the Brillouin zone at $L_y = 8$ for the Fermi liquid (FL, left side) versus the CFL (right side). The FL has an almost circular Fermi sea with radius k_F (gray dashed circle), whereas the CFL occupations are featureless. (b) Connected structure factor $S(\mathbf{q}) = \langle \hat{\rho}_{\mathbf{q}} \hat{\rho}_{-\mathbf{q}} \rangle - \langle \hat{\rho}_{\mathbf{q}} \rangle \langle \hat{\rho}_{-\mathbf{q}} \rangle$ at $L_y = 8$. Characteristic features of a Fermi surface are visible for both the FL and CFL: near-vanishing weight outside $|\mathbf{q}| \approx 2k_F$, and peaks corresponding to momentum transfers inside that radius. Qualitative differences are due to, e.g., strong scattering to higher Brillouin zones for the FL. (c) Cuts of $S(\mathbf{q})$ at constant q_y for $L_y = 5$ for the CFL. Each peak or inflection in $S(\mathbf{q})$ quantitatively matches scattering events across the almost-circular composite Fermi surface (Inset). Parameters: $\epsilon_r = 6, 60$ for the FL and CFL respectively, $(\theta, d) = (3.89^\circ, 100 \text{ \AA})$, and bond dimension $\chi = 2048 - 4096$.

composite fermion, and \mathbf{k}_i fill a Fermi sea. Note that while continuous translation symmetry fixes $\psi_{\mathbf{k}}^{\text{CF}}(\mathbf{r}) = e^{i\mathbf{k}\cdot\mathbf{r}}$ in the LLL, different Bloch states may be used for systems with lattice translation symmetry.

The common construction of composite fermions in the LLL, involving attaching 4π flux of an emergent gauge field to the electrons in order to cancel the magnetic flux, is at odds with the fact that the TMD electrons experience no magnetic flux. To address this, and physically interpret the wavefunction (4), we develop a parton description. We fractionalize the electron as $\psi_l = \phi\chi_l$, where the fermion ϕ carries the charge and the boson χ describes the layer structure. There is a gauge re-

dundancy described by an $U(1)$ gauge field α_μ under which ϕ and χ have opposite charges. Motivated by the nearly-vortexable character of the low-energy wavefunctions (3), we condense χ into the state $\zeta_l(\mathbf{r})$ such that α_μ has an average flux of 2π per unit cell. The corresponding Gutzwiller-projected electron wavefunction is of the form $\Psi = \Psi_\phi \prod_i \zeta_i$, where Ψ_ϕ is now a wavefunction of flux-feeling particles. Substituting the Rezayi-Read ansatz for Ψ_ϕ , we arrive at (4) again.

Experimental Signatures.— We now discuss the experimental implications of our work, including a phase diagram in twist angle and displacement field, an optical probe of the almost-ideal band geometry, and experimental probes of the CFL state.

Fig. 3(a) shows the phase diagram at $\nu = -1$ as a function of displacement field within two-valley iDMRG for the top valence band at $(\theta, \epsilon_r, d, L_y) = (3.7^\circ, 6, 100 \text{ \AA}, 6)$. We find that valley polarization (VP) persists to $V \sim 30$ meV — consistent with experiments [26] that have observed valley polarization up to 125 mV/nm — before giving rise to a non-valley polarized (NVP) phase [96]. Inside the VP regime, the top valence band undergoes a $C = 1 \rightarrow 0$ topological transition at $V \sim 20$ meV, so we expect a small intermediate topologically trivial phase (blue hashes) near this angle.

We then study the phase diagram at $\nu = -1/2$ via ED in Fig. 3(b) with $(\epsilon_r, d) = (8, 300 \text{ \AA})$, focusing on the topologically nontrivial regime, and assuming valley polarization throughout. Around the representative points discussed above in ED and DMRG, we see a broad CFL phase centered around 3.6° — in line with expectations from $\nu = -1, 0$ bandwidths. The CFL competes with an ordinary FL that sets in at sufficiently large V . A similar phase diagram for $\nu = -3/4$ is shown in the SM, with a CFL phase that is more sensitive to displacement field.

Before tuning to experimental signatures of CFLs, we discuss an optical probe of ideal quantum geometry for FCIs and CFLs. In particular, we show that vortexable bands only have interband optical transitions under right-circularly polarized light. The left-circular response is extinguished by the quantum geometry, meaning that ideal geometry implies perfect circular dichroism:

$$\frac{\sigma^+ - \sigma^-}{\sigma^+ + \sigma^-} = 1; \quad \sigma^\pm(\omega) = \frac{ie^2}{\hbar} \sum_{\mathbf{k}, a \neq b=0} \frac{f_{ab}}{\epsilon_{ab}} \frac{|\langle \psi_{\mathbf{k}a} | \hat{v}^\pm | \psi_{\mathbf{k}b} \rangle|^2}{\omega - \epsilon_{ab}}. \quad (5)$$

Here ϵ_a are band energies, $\epsilon_{ab} = \epsilon_a - \epsilon_b$ are their differences, $f_{ab} = f(\epsilon_a) - f(\epsilon_b)$ are Fermi factors, and $\hat{v}^\pm = -i[\hat{x} \pm i\hat{y}, \hat{H}]$ is the velocity operator. The vortexability condition $\hat{z}P = P\hat{z}P$ means that the matrix elements $(I - P)\hat{v}^+P$ associated with the left-circularly polarized light uniformly vanish. Fig. 3(c) shows how this manifests in the $\nu = -1$ state. As the $C = +1$ band is nearly vortexable, the left-circular signals from the second and third valence bands to the top valence band (above the dashed Fermi level) nearly vanish, resulting in circular dichroism > 0.9 at resonance. As a “control ex-

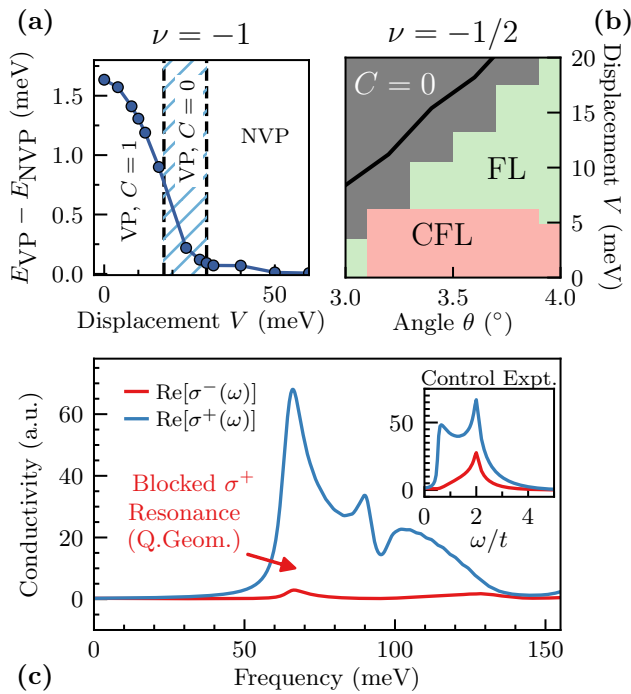


FIG. 3. Many-body phase diagrams and optical responses. (a) Phase diagram at $\nu = -1$ and twist angle 3.7° showing a topological transition of the top valence band from $C = 1$ to $C = 0$ (first dashed line) while retaining valley polarization. Valley polarization is subsequently lost at larger displacement fields (second dashed line). (b) Phase diagram of the topological regime at $\nu = -1/2$: the large extent of the CFL phase is shown in red. The green regions correspond to Fermi liquid states, and the gray regions are near or past the $C = 1 \rightarrow 0$ topological transition marked with a black line. (c) Direct optical probe of almost-ideal quantum geometry via an “extinguished” valence-valence optical responses in σ^- . We compute optical response for the $\nu = -1$ SCHF bandstructure of Fig. 1b at $(\theta, \epsilon_r, V) = (3.89^\circ, 8, 0)$. Inset: “control experiment” showing non-vanishing σ^+, σ^- resonances in the Haldane hexagon model with topological $C = \pm 1$ bands but non-ideal quantum geometry.

periment” we examine the Haldane model Haldane model at $(t, t_2) = (1, 0.05)$. This has Chern bands $C = \pm 1$, but non-ideal quantum geometry, so we find conductivity is roughly comparable for both circular polarizations (see inset). Observing this effect — which reflects the quality of the quantum geometry rather than topology — likely requires a large sample of high quality (uniform twist angle, low strain, etc), but does not require low temperature. We note that SCHF typically overestimates the gap at $\nu = 1$, since it neglects, for instance, the effects of disorder.

Lastly, we discuss direct experimental probes of the zero-field CFL. While the CFL and the FL are both compressible and metallic, they differ in that the CFL’s excitations have vanishing overlap with the electron in the limit of low energies, and CFs themselves are best thought of as (doubled) *vortices* in the electronic fluid

[3, 4, 97–99]. This observation leads to a number of striking physical responses that differ strongly from Fermi liquids. These include (i) a “pseudogap” in the tunneling density of states $A(\omega) \propto e^{-\omega_0/\omega}$ [100] as a function of bias ω , which has been observed between two CFLs with a tunnel barrier [5]; (ii) distinct DC conductivity in the clean limit: $\sigma_{xx} \rightarrow 0$ in a CFL in the absence of disorder $k_F l \rightarrow \infty$, whereas in the FL, even in a Chern band, σ_{xx} diverges [101]; (iii) strong violation of the Wiedemann-Franz law [98, 99] which compares heat and charge transport; (iv) quantum oscillations with doping, associated with the fact that CFs feel a magnetic field $\propto (\nu - 1/2)$ and can fill Landau levels, leading to Jain-like [1] FCI’s when fully developed, which can further be probed using geometric resonance with a one-dimensional periodic grating [3, 6, 7]; (v) vanishing thermoelectric conductance $\alpha_{xx} = j_x / (-\partial_x T)$ due to approximate emergent particle-hole symmetry [102, 103]; (vi) surface acoustic wave attenuation, a contactless probe that measures $\sigma_{xx}(\mathbf{q}) \propto |\mathbf{q}|$ in the CFL [3], as opposed to $\sigma_{xx} \propto |\mathbf{q}|^{-1}$ in a clean FL [8].

Finally we highlight unique aspects of zero field CFLs in moiré materials that are absent in the Landau level realization. First, note the large effective magnetic fields. The Chern bands of MoTe_2 effectively host a single magnetic flux quantum per moiré unit cell, which at a twist angle of 3.7° translate into an effective magnetic field of 160 T, clearly exceeding typical laboratory magnetic fields, and leading to enhanced energy scales. The lack of *real* quantizing magnetic fields, however, opens up the possibility of employing zero field experimental probes such as high resolution angle resolved photo-emission spectroscopy (ARPES). Further, the exponentially suppressed tunneling density of states of the CFL could be probed through tunneling from a proximate Fermi liquid state, or via spatial variation of the displacement field which can be used to create a CFL-FL interface within the same sample. Furthermore, our work does not rule out the possibility of a continuous quantum phase transition, driven by displacement field, between the CFL and FL [90], which could be studied experimentally. Since the effective magnetic field of the TMD originates from spontaneous symmetry breaking of time reversal symmetry through valley polarization, rather than external B field application, domains between opposite valley polarizations and hence between time-reversal-related CFLs are expected. Transport properties across such a domain wall would interrogate composite fermions in an entirely new regime, and potentially shed light on their proposed Dirac character [4, 97, 99]. Finally, we note that moiré phonons occur on the same scale as the effective magnetic length in this system; their interplay with CFL physics is unclear at present and worthy of future study.

Acknowledgements.—We thank Junyeong Ahn, Ilya Esterlis, Eslam Khalaf, Jiaqi Cai and especially Bertrand Halperin for helpful discussions. We acknowledge Michael Zaletel, Tomohiro Soejima, and Johannes Hauschild for ongoing and related collaborations. A.V.

is supported by the Simons Collaboration on Ultra-Quantum Matter, which is a grant from the Simons Foun-

ation (651440, A.V.). This research is funded in part by the Gordon and Betty Moore Foundation's EPiQS Initiative, Grant GBMF8683 to D.E.P.

-
- [1] J. K. Jain, *Phys. Rev. Lett.* **63**, 199 (1989).
- [2] A. Lopez and E. Fradkin, *Phys. Rev. B* **44**, 5246 (1991).
- [3] B. I. Halperin, P. A. Lee, and N. Read, *Phys. Rev. B* **47**, 7312 (1993).
- [4] D. T. Son, *Phys. Rev. X* **5**, 031027 (2015).
- [5] J. P. Eisenstein, L. N. Pfeiffer, and K. W. West, *Phys. Rev. Lett.* **69**, 3804 (1992).
- [6] R. L. Willett, R. R. Ruel, K. W. West, and L. N. Pfeiffer, *Phys. Rev. Lett.* **71**, 3846 (1993).
- [7] W. Kang, H. L. Stormer, L. N. Pfeiffer, K. W. Baldwin, and K. W. West, *Phys. Rev. Lett.* **71**, 3850 (1993).
- [8] R. L. Willett, R. R. Ruel, M. A. Paalanen, K. W. West, and L. N. Pfeiffer, *Phys. Rev. B* **47**, 7344 (1993).
- [9] V. J. Goldman, B. Su, and J. K. Jain, *Phys. Rev. Lett.* **72**, 2065 (1994).
- [10] J. H. Smet, D. Weiss, R. H. Blick, G. Lütjering, K. von Klitzing, R. Fleischmann, R. Ketzmerick, T. Geisel, and G. Weimann, *Phys. Rev. Lett.* **77**, 2272 (1996).
- [11] N. Read and D. Green, *Phys. Rev. B* **61**, 10267 (2000).
- [12] Y. Tang, L. Li, T. Li, Y. Xu, S. Liu, K. Barmak, K. Watanabe, T. Taniguchi, A. H. MacDonald, J. Shan, and K. F. Mak, *Nature* **579**, 353 (2020).
- [13] Y. Xu, K. Kang, K. Watanabe, T. Taniguchi, K. F. Mak, and J. Shan, *Nature Nanotechnology* **17**, 934 (2022).
- [14] L. Wang, E.-M. Shih, A. Ghiotto, D. A. R. L. Xian, C. Tan, M. Claassen, D. M. Kennes, Y. Bai, B. Kim, K. Watanabe, T. Taniguchi, X. Zhu, J. Hone, A. Rubio, A. N. Pasupathy, and C. R. Dean, *Nature Materials* **19**, 861 (2020).
- [15] Y. Xu, S. Liu, D. A. Rhodes, K. Watanabe, T. Taniguchi, J. Hone, V. Elser, K. F. Mak, and J. Shan, *Nature* **587**, 214 (2020).
- [16] X. Huang, T. Wang, S. Miao, C. Wang, Z. Li, Z. Lian, T. Taniguchi, K. Watanabe, S. Okamoto, D. Xiao, S.-F. Shi, and Y.-T. Cui, *Nature Physics* **17**, 715 (2021).
- [17] E. C. Regan, D. Wang, C. Jin, M. I. Bakti Utama, B. Gao, X. Wei, S. Zhao, W. Zhao, Z. Zhang, K. Yumigeta, M. Blei, J. D. Carlström, K. Watanabe, T. Taniguchi, S. Tongay, M. Crommie, A. Zettl, and F. Wang, *Nature* **579**, 359 (2020).
- [18] T. Li, S. Jiang, L. Li, Y. Zhang, K. Kang, J. Zhu, K. Watanabe, T. Taniguchi, D. Chowdhury, L. Fu, J. Shan, and K. F. Mak, *Nature* **597**, 350 (2021).
- [19] A. Ghiotto, E.-M. Shih, G. S. S. G. Pereira, D. A. Rhodes, B. Kim, J. Zang, A. J. Millis, K. Watanabe, T. Taniguchi, J. C. Hone, L. Wang, C. R. Dean, and A. N. Pasupathy, *Nature* **597**, 345 (2021).
- [20] T. Li, S. Jiang, B. Shen, Y. Zhang, L. Li, Z. Tao, T. Devakul, K. Watanabe, T. Taniguchi, L. Fu, J. Shan, and K. F. Mak, *Nature* **600**, 641 (2021).
- [21] W. Zhao, K. Kang, L. Li, C. Tschirhart, E. Redekop, K. Watanabe, T. Taniguchi, A. Young, J. Shan, and K. F. Mak, "Realization of the haldane chern insulator in a moiré lattice," (2022), [arXiv:2207.02312 \[cond-mat.mes-hall\]](https://arxiv.org/abs/2207.02312).
- [22] Z. Tao, B. Shen, S. Jiang, T. Li, L. Li, L. Ma, W. Zhao, J. Hu, K. Pistunova, K. Watanabe, T. Taniguchi, T. F. Heinz, K. F. Mak, and J. Shan, "Valley-coherent quantum anomalous hall state in ab-stacked mote2/wse2 bilayers," (2022), [arXiv:2208.07452 \[cond-mat.mes-hall\]](https://arxiv.org/abs/2208.07452).
- [23] B. A. Foutty, J. Yu, T. Devakul, C. R. Kometter, Y. Zhang, K. Watanabe, T. Taniguchi, L. Fu, and B. E. Feldman, *Nature Materials* (2023), [10.1038/s41563-023-01534-z](https://doi.org/10.1038/s41563-023-01534-z).
- [24] B. A. Foutty, C. R. Kometter, T. Devakul, A. P. Reddy, K. Watanabe, T. Taniguchi, L. Fu, and B. E. Feldman, "Mapping twist-tuned multi-band topology in bilayer wse₂," (2023), [arXiv:2304.09808 \[cond-mat.mes-hall\]](https://arxiv.org/abs/2304.09808).
- [25] E. Anderson, F.-R. Fan, J. Cai, W. Holtzmann, T. Taniguchi, K. Watanabe, D. Xiao, W. Yao, and X. Xu, "Programming correlated magnetic states via gate controlled moiré geometry," (2023), [arXiv:2303.17038 \[cond-mat.mes-hall\]](https://arxiv.org/abs/2303.17038).
- [26] J. Cai, E. Anderson, C. Wang, X. Zhang, X. Liu, W. Holtzmann, Y. Zhang, F. Fan, T. Taniguchi, K. Watanabe, Y. Ran, T. Cao, L. Fu, D. Xiao, W. Yao, and X. Xu, [arXiv e-prints](https://arxiv.org/abs/2304.08470), [arXiv:2304.08470 \(2023\)](https://arxiv.org/abs/2304.08470), [arXiv:2304.08470 \[cond-mat.mes-hall\]](https://arxiv.org/abs/2304.08470).
- [27] Y. Zeng, Z. Xia, K. Kang, J. Zhu, P. Knüppel, C. Vaswani, K. Watanabe, T. Taniguchi, K. F. Mak, and J. Shan, [arXiv e-prints](https://arxiv.org/abs/2305.00973), [arXiv:2305.00973 \(2023\)](https://arxiv.org/abs/2305.00973), [arXiv:2305.00973 \[cond-mat.mes-hall\]](https://arxiv.org/abs/2305.00973).
- [28] F. Wu, T. Lovorn, E. Tutuc, and A. H. MacDonald, *Phys. Rev. Lett.* **121**, 026402 (2018).
- [29] F. Wu, T. Lovorn, E. Tutuc, I. Martin, and A. H. MacDonald, *Phys. Rev. Lett.* **122**, 086402 (2019).
- [30] H. Yu, M. Chen, and W. Yao, *National Science Review* **7**, 12 (2019).
- [31] D. Zhai and W. Yao, *Phys. Rev. Mater.* **4**, 094002 (2020).
- [32] H. Tang, S. Carr, and E. Kaxiras, *Physical Review B* **104** (2021), [10.1103/physrevb.104.155415](https://doi.org/10.1103/physrevb.104.155415).
- [33] T. Devakul, V. Crépel, Y. Zhang, and L. Fu, *Nature Communications* **12** (2021), [10.1038/s41467-021-27042-9](https://doi.org/10.1038/s41467-021-27042-9).
- [34] Y. Zhang, T. Devakul, and L. Fu, *Proceedings of the National Academy of Sciences* **118** (2021), [10.1073/pnas.2112673118](https://doi.org/10.1073/pnas.2112673118).
- [35] Y.-H. Zhang, D. Sheng, and A. Vishwanath, *Physical Review Letters* **127** (2021), [10.1103/physrevlett.127.247701](https://doi.org/10.1103/physrevlett.127.247701).
- [36] J. Zang, J. Wang, J. Cano, and A. J. Millis, *Phys. Rev. B* **104**, 075150 (2021).
- [37] J. Wang, J. Zang, J. Cano, and A. J. Millis, "Staggered pseudo magnetic field in twisted transition metal dichalcogenides: Physical origin and experimental consequences," (2021), [arXiv:2110.14570 \[cond-mat.mes-hall\]](https://arxiv.org/abs/2110.14570).
- [38] J. Zang, J. Wang, J. Cano, A. Georges, and A. J. Millis, *Phys. Rev. X* **12**, 021064 (2022).
- [39] H. Pan, F. Wu, and S. Das Sarma, *Phys. Rev. Res.* **2**, 033087 (2020).

- [40] A. Abouelkomsan, E. J. Bergholtz, and S. Chatterjee, “Multiferroicity and topology in twisted transition metal dichalcogenides,” (2022), [arXiv:2210.14918 \[cond-mat.str-el\]](#).
- [41] V. Crépel, N. Regnault, and R. Queiroz, “The chiral limits of moiré semiconductors: origin of flat bands and topology in twisted transition metal dichalcogenides homobilayers,” (2023), [arXiv:2305.10477 \[cond-mat.mes-hall\]](#).
- [42] S. A. Parameswaran, R. Roy, and S. L. Sondhi, *Comptes Rendus Physique* **14**, 816 (2013).
- [43] T. Neupert, C. Chamon, T. Iadecola, L. H. Santos, and C. Mudry, *Physica Scripta* **T164**, 014005 (2015).
- [44] E. J. BERGHOLTZ and Z. LIU, *International Journal of Modern Physics B* **27**, 1330017 (2013), <https://doi.org/10.1142/S021797921330017X>.
- [45] Z. Liu and E. J. Bergholtz, in *Reference Module in Materials Science and Materials Engineering* (Elsevier, 2023).
- [46] H. Li, U. Kumar, K. Sun, and S.-Z. Lin, *Phys. Rev. Research* **3**, L032070 (2021).
- [47] V. Crépel and L. Fu, *Phys. Rev. B* **107**, L201109 (2023).
- [48] N. Morales-Durán, J. Wang, G. R. Schleder, M. Angeli, Z. Zhu, E. Kaxiras, C. Repellin, and J. Cano, *arXiv e-prints*, [arXiv:2304.06669 \(2023\)](#), [arXiv:2304.06669 \[cond-mat.str-el\]](#).
- [49] C. Wang, X.-W. Zhang, X. Liu, Y. He, X. Xu, Y. Ran, T. Cao, and D. Xiao, *arXiv e-prints*, [arXiv:2304.11864 \(2023\)](#), [arXiv:2304.11864 \[cond-mat.str-el\]](#).
- [50] A. P. Reddy, F. F. Alsallom, Y. Zhang, T. Devakul, and L. Fu, *arXiv e-prints*, [arXiv:2304.12261 \(2023\)](#), [arXiv:2304.12261 \[cond-mat.mes-hall\]](#).
- [51] E. M. Spanton, A. A. Zibrov, H. Zhou, T. Taniguchi, K. Watanabe, M. P. Zaletel, and A. F. Young, *Science* **360**, 62 (2018).
- [52] A. Kol and N. Read, *Phys. Rev. B* **48**, 8890 (1993).
- [53] Y. Cao, V. Fatemi, A. Demir, S. Fang, S. L. Tomarken, J. Y. Luo, J. D. Sanchez-Yamagishi, K. Watanabe, T. Taniguchi, E. Kaxiras, R. C. Ashoori, and P. Jarillo-Herrero, *Nature* **556**, 80 (2018).
- [54] Y. Cao, V. Fatemi, S. Fang, K. Watanabe, T. Taniguchi, E. Kaxiras, and P. Jarillo-Herrero, *Nature* **556**, 43 (2018).
- [55] A. L. Sharpe, E. J. Fox, A. W. Barnard, J. Finney, K. Watanabe, T. Taniguchi, M. A. Kastner, and D. Goldhaber-Gordon, *Science* **365**, 605 (2019).
- [56] M. Serlin, C. L. Tschirhart, H. Polshyn, Y. Zhang, J. Zhu, K. Watanabe, T. Taniguchi, L. Balents, and A. F. Young, *Science* **367**, 900 (2020).
- [57] P. J. Ledwith, G. Tarnopolsky, E. Khalaf, and A. Vishwanath, *Phys. Rev. Research* **2**, 023237 (2020).
- [58] A. Abouelkomsan, K. Yang, and E. J. Bergholtz, *arXiv e-prints*, [arXiv:2202.10467 \(2022\)](#), [arXiv:2202.10467 \[cond-mat.str-el\]](#).
- [59] C. Repellin and T. Senthil, *Phys. Rev. Research* **2**, 023238 (2020).
- [60] Y. Xie, A. T. Pierce, J. M. Park, D. E. Parker, E. Khalaf, P. Ledwith, Y. Cao, S. H. Lee, S. Chen, P. R. Forrester, K. Watanabe, T. Taniguchi, A. Vishwanath, P. Jarillo-Herrero, and A. Yacoby, *Nature* **600**, 439 (2021).
- [61] D. Parker, P. Ledwith, E. Khalaf, T. Soejima, J. Hauschild, Y. Xie, A. Pierce, M. P. Zaletel, A. Yacoby, and A. Vishwanath, *arXiv preprint arXiv:2112.13837* (2021).
- [62] S. D. Geraedts, M. P. Zaletel, R. S. K. Mong, M. A. Metlitski, A. Vishwanath, and O. I. Motrunich, *Science* **352**, 197 (2016).
- [63] N. Regnault and B. A. Bernevig, *Phys. Rev. X* **1**, 021014 (2011).
- [64] A. G. Grushin, T. Neupert, C. Chamon, and C. Mudry, *Physical Review B* **86**, 205125 (2012).
- [65] For example, in twisted bilayer graphene the single peak of charge density at AA sites gives a sharp Hartree peak, dramatically increasing the total bandwidth at fillings with a single active band [104]. In contrast, spin-valley locking in TMDs naturally isolates a single Chern band. Here charge density is doubly-peaked, so the interaction-generated dispersion is mild [105] — and almost perfectly cancels against the non-interacting dispersion. See also [44, 58, 106, 107].
- [66] R. Roy, *Phys. Rev. B* **90**, 165139 (2014).
- [67] T. S. Jackson, G. Möller, and R. Roy, *Nature Communications* **6**, 8629 (2015).
- [68] M. Claassen, C. H. Lee, R. Thomale, X.-L. Qi, and T. P. Devereaux, *Phys. Rev. Lett.* **114**, 236802 (2015).
- [69] G. Tarnopolsky, A. J. Kruchkov, and A. Vishwanath, *Phys. Rev. Lett.* **122**, 106405 (2019).
- [70] T. Ozawa and B. Mera, *Phys. Rev. B* **104**, 045103 (2021).
- [71] B. Mera and T. Ozawa, *Phys. Rev. B* **104**, 045104 (2021).
- [72] B. Mera and T. Ozawa, *Phys. Rev. B* **104**, 115160 (2021).
- [73] J. Wang, J. Cano, A. J. Millis, Z. Liu, and B. Yang, *Phys. Rev. Lett.* **127**, 246403 (2021).
- [74] J. Wang and Z. Liu, *Phys. Rev. Lett.* **128**, 176403 (2022).
- [75] P. J. Ledwith, A. Vishwanath, and D. E. Parker, *arXiv e-prints*, [arXiv:2209.15023 \(2022\)](#), [arXiv:2209.15023 \[cond-mat.str-el\]](#).
- [76] J. Wang, S. Klevtsov, and Z. Liu, *arXiv e-prints*, [arXiv:2210.13487 \(2022\)](#), [arXiv:2210.13487 \[cond-mat.mes-hall\]](#).
- [77] J. Dong, P. J. Ledwith, E. Khalaf, J. Y. Lee, and A. Vishwanath, *arXiv e-prints*, [arXiv:2210.13477 \(2022\)](#), [arXiv:2210.13477 \[cond-mat.mes-hall\]](#).
- [78] D. Varjas, A. Abouelkomsan, K. Yang, and E. J. Bergholtz, *SciPost Phys.* **12**, 118 (2022).
- [79] P. J. Ledwith, A. Vishwanath, and E. Khalaf, *Phys. Rev. Lett.* **128**, 176404 (2022).
- [80] S. A. Trugman and S. Kivelson, *Phys. Rev. B* **31**, 5280 (1985).
- [81] S. D. Geraedts, J. Wang, E. H. Rezayi, and F. D. M. Haldane, *Phys. Rev. Lett.* **121**, 147202 (2018).
- [82] X.-L. Qi, *Phys. Rev. Lett.* **107**, 126803 (2011).
- [83] D. E. Parker, X. Cao, and M. P. Zaletel, *Phys. Rev. B* **102**, 035147 (2020).
- [84] T. Soejima, D. E. Parker, N. Bultinck, J. Hauschild, and M. P. Zaletel, *Phys. Rev. B* **102**, 205111 (2020).
- [85] The in-principle possibility of a highly non-circular CFS outside of the LLL setting is therefore not realized here.
- [86] Y.-M. Lu and Y. Ran, *Physical Review B* **85**, 165134 (2012).
- [87] J. McGreevy, B. Swingle, and K.-A. Tran, *Physical Review B* **85**, 125105 (2012).
- [88] G. Murthy and R. Shankar, “Composite Fermions for Fractionally Filled Chern Bands,” (2011),

- arxiv:1108.5501 [cond-mat].
- [89] G. Murthy and R. Shankar, *Physical Review B* **86**, 195146 (2012).
- [90] M. Barkeshli and J. McGreevy, *Physical Review B* **86**, 075136 (2012).
- [91] M. Barkeshli and J. McGreevy, *Physical Review B* **89**, 235116 (2014).
- [92] J. Dong, J. Wang, and L. Fu, arXiv e-prints, arXiv:2208.10516 (2022), arXiv:2208.10516 [cond-mat.mes-hall].
- [93] B. Estienne, N. Regnault, and V. Crépel, arXiv e-prints, arXiv:2304.01251 (2023), arXiv:2304.01251 [cond-mat.mes-hall].
- [94] J. Wang, Y. Zheng, A. J. Millis, and J. Cano, *Phys. Rev. Research* **3**, 023155 (2021).
- [95] E. Rezayi and N. Read, *Physical Review Letters* **72**, 900 (1994).
- [96] The phase boundary is determined when the energy difference is less than 1 K.
- [97] M. A. Metlitski and A. Vishwanath, *Physical Review B* **93** (2016), 10.1103/physrevb.93.245151.
- [98] C. Wang and T. Senthil, *Phys. Rev. B* **94**, 245107 (2016).
- [99] C. Wang and T. Senthil, *Phys. Rev. B* **93**, 085110 (2016).
- [100] S. He, P. M. Platzman, and B. I. Halperin, *Phys. Rev. Lett.* **71**, 777 (1993).
- [101] N. Nagaosa, J. Sinova, S. Onoda, A. H. MacDonald, and N. P. Ong, *Rev. Mod. Phys.* **82**, 1539 (2010).
- [102] A. C. Potter, M. Serbyn, and A. Vishwanath, *Physical Review X* **6** (2016), 10.1103/physrevx.6.031026.
- [103] C. Wang, N. R. Cooper, B. I. Halperin, and A. Stern, *Phys. Rev. X* **7**, 031029 (2017).
- [104] D. Parker, P. Ledwith, E. Khalaf, T. Soejima, J. Hauschild, Y. Xie, A. Pierce, M. P. Zaletel, A. Yacoby, and A. Vishwanath, arXiv e-prints, arXiv:2112.13837 (2021), arXiv:2112.13837 [cond-mat.str-el].
- [105] Q. Gao, J. Dong, P. Ledwith, D. Parker, and E. Khalaf, “Untwisting moiré physics: Almost ideal bands and fractional chern insulators in periodically strained monolayer graphene,” (2022), arXiv:2211.00658 [cond-mat.mes-hall].
- [106] A. M. Läuchli, Z. Liu, E. J. Bergholtz, and R. Moessner, *Phys. Rev. Lett.* **111**, 126802 (2013).
- [107] Z. Liu and E. J. Bergholtz, *Physical Review B* **87**, 035306 (2013).
- [108] N. Bultinck, E. Khalaf, S. Liu, S. Chatterjee, A. Vishwanath, and M. P. Zaletel, *Phys. Rev. X* **10**, 031034 (2020).
- [109] O. Vafek and J. Kang, *Phys. Rev. Lett.* **125**, 257602 (2020).
- [110] E. H. Rezayi and F. D. M. Haldane, *Phys. Rev. Lett.* **84**, 4685 (2000).
- [111] F. D. M. Haldane and E. H. Rezayi, *Phys. Rev. B* **31**, 2529 (1985).
- [112] F. D. M. Haldane, *Phys. Rev. Lett.* **55**, 2095 (1985).
- [113] J. Wang, S. D. Geraedts, E. H. Rezayi, and F. D. M. Haldane, *Phys. Rev. B* **99**, 125123 (2019).
- [114] J. Shao, E.-A. Kim, F. D. M. Haldane, and E. H. Rezayi, *Phys. Rev. Lett.* **114**, 206402 (2015).
- [115] J. Wang, *Phys. Rev. Lett.* **122**, 257203 (2019).
- [116] F. D. M. Haldane, *Journal of Mathematical Physics* **59**, 081901 (2018), <https://doi.org/10.1063/1.5046122>.

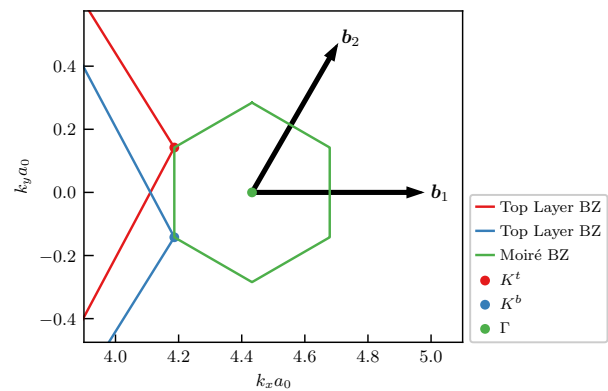


FIG. 4. Geometry of the moiré Brillouin zone.

- [117] F. D. M. Haldane, *Journal of Mathematical Physics* **59**, 071901 (2018), <https://doi.org/10.1063/1.5042618>.
- [118] J. K. Jain and R. K. Kamilla, *Phys. Rev. B.* **55**, R4895(R) (1997).
- [119] D. E. Parker, T. Soejima, J. Hauschild, M. P. Zaletel, and N. Bultinck, *Phys. Rev. Lett.* **127**, 027601 (2021).
- [120] T. Wang, D. E. Parker, T. Soejima, J. Hauschild, S. Anand, N. Bultinck, and M. P. Zaletel, arXiv preprint arXiv:2211.02693 (2022).
- [121] D. Vanderbilt, *Berry Phases in Electronic Structure Theory: Electric Polarization, Orbital Magnetization and Topological Insulators* (Cambridge University Press, 2018).
- [122] B. Pirvu, V. Murg, J. I. Cirac, and F. Verstraete, *New Journal of Physics* **12**, 025012 (2010).
- [123] D. Varjas, M. P. Zaletel, and J. E. Moore, *Physical Review B* **88**, 155314 (2013).
- [124] X.-Y. Song, H. Goldman, and L. Fu, “Emergent qed₃ from half-filled flat chern bands,” (2023), arXiv:2302.10169 [cond-mat.str-el].

Appendix A: Continuum Model

In this Appendix we review the continuum model of TMDs [29].

Moiré Geometry. We take monolayer TMD lattice vectors

$$\mathbf{R}_{1,2} = a_0 \left(\frac{1}{2}, \mp \frac{\sqrt{3}}{2} \right), \quad \mathbf{G}_{1,2} = \frac{2\pi}{a_0} \left(1, \mp \frac{1}{\sqrt{3}} \right) \quad (\text{A1})$$

where $a_0 = 3.52 \text{ \AA}$ is the monolayer TMD lattice constant [49].

As usual, the moiré Brillouin zone for the K -valley has moiré lattice vectors

$$\mathbf{a}_1 = \frac{a_0}{2 \sin \frac{\theta}{2}} \left(\frac{\sqrt{3}}{2}, -\frac{1}{2} \right), \quad \mathbf{a}_2 = \frac{a_0}{2 \sin \frac{\theta}{2}} (0, 1), \quad (\text{A2})$$

$$\mathbf{b}_1 = \frac{8\pi \sin \frac{\theta}{2}}{\sqrt{3}a_0} (1, 0), \quad \mathbf{b}_j = R_{(j-1)\pi/3} \mathbf{b}_1 \quad (\text{A3})$$

where R_θ is a rotation matrix. The geometry is shown in Fig. 4, where one can see that two of the vertices of the hexagonal moiré Brillouin zone match the rotated K -points of the monolayer TMD:

$$\mathbf{K}^\ell = R_{\ell\theta/2}\mathbf{K}, \quad \mathbf{K} = \frac{1}{3}\mathbf{G}_1 + \frac{1}{3}\mathbf{G}_2 \quad (\text{A4})$$

We often consider a commensurate angle $\theta = 3.89^\circ$.

Single-Particle Model. The continuum model for a moiré bilayer TMD [29] consists of four species of electrons, corresponding to two layers in each valley. Since the band gap from the valence band to the conduction band is large, the conduction bands are integrated out. Furthermore, due to spin-orbit coupling, the spin degree of freedom is locked to the valley degree of freedom: valence electrons at the K valley have spin up, and valence electrons at the K' valley have spin down. After these approximations, each valley has two degrees of freedom one for each layer. We focus on the K -valley and obtain the K' valley by time-reversal, described below.

The single-particle Hamiltonian for holes in the K -valley is

$$h_K = \begin{bmatrix} h^b(\mathbf{r}) + V/2 & T(\mathbf{r}) \\ T^\dagger(\mathbf{r}) & h^t(\mathbf{r}) - V/2 \end{bmatrix} \quad (\text{A5})$$

This Hamiltonian consists of three parts: the standard kinetic term, the moiré potentials and tunnelings and the displacement field. The kinetic part is

$$h_{\text{kin}} = \begin{bmatrix} -\frac{(\mathbf{p} - \hbar v_F \mathbf{K}^b)^2}{2m^*} & 0 \\ 0 & -\frac{(\mathbf{p} - \hbar v_F \mathbf{K}^t)^2}{2m^*} \end{bmatrix} \quad (\text{A6})$$

and the moiré potential and tunnelings are

$$h_{\text{moire}} = \begin{bmatrix} \Delta^b(\mathbf{r}) & T(\mathbf{r}) \\ T^\dagger(\mathbf{r}) & \Delta^t(\mathbf{r}) \end{bmatrix} \quad (\text{A7a})$$

$$\Delta^\ell(\mathbf{r}) = 2v \sum_{j=1,3,5} \cos(\mathbf{b}_j \cdot \mathbf{r} + \ell\psi), \quad (\text{A7b})$$

$$T(\mathbf{r}) = w(1 + e^{i\mathbf{b}_2 \cdot \mathbf{r}} + e^{i\mathbf{b}_3 \cdot \mathbf{r}}). \quad (\text{A7c})$$

Fig. 5(a) shows the bandstructure of Eq. (A5) at $V = 0$. As mentioned in the main text, we take parameters from recent first principles calculations of MoTe₂ [49]: $(a_0, m^*, V, \psi, \omega) = (3.52 \text{ \AA}, 0.6m_e, 20.8 \text{ meV}, -107.7^\circ, -23.8 \text{ meV})$ at $\theta = 3.89^\circ$ (see also [29, 41, 50]). At these parameters, the top valence band for this model has Chern number $C = +1$, and the second-to-top band has Chern number $C = -1$.

Symmetries. Some key symmetries of Eq. (A5) without displacement field are C_3 , C_{2y} , and time-reversal \mathcal{T} . We give their action after applying a unitary transform to make their action simpler. Let $\tau = K, K' = 1, -1$ index valleys and define

$$h'_\tau(\mathbf{r}) = U_\tau(\mathbf{r})h_\tau(\mathbf{r})U_\tau^\dagger(\mathbf{r}), U_\tau(\mathbf{r}) = \begin{bmatrix} e^{-i\tau\mathbf{K}^b \cdot \mathbf{r}} & 0 \\ 0 & e^{-i\tau\mathbf{K}^t \cdot \mathbf{r}} \end{bmatrix}. \quad (\text{A8})$$

Then symmetries then act on h' as follows:

$$C_3 h'_\tau(\mathbf{r}) C_3^{-1} = h'_\tau(e^{\frac{2\pi i}{3}\ell_y \mathbf{r}}), \quad (\text{A9a})$$

$$C_{2y} h'_\tau(x, y) (C_{2y})^{-1} = \ell_x h'_{-\tau}(-x, y) \ell_x, \quad (\text{A9b})$$

$$\mathcal{T} h'_\tau(x, y) \mathcal{T}^{-1} = h'_{-\tau}(x, y)^*, \quad (\text{A9c})$$

where we use layer-space Pauli matrices $\ell_{0,x,y,z}$.

Interactions. Consider creation operators

$$\hat{c}_{\mathbf{k}\tau b}^\dagger |0\rangle = |\psi_{\mathbf{k}\tau b}\rangle, \quad \hat{h}_\tau(\mathbf{k}) |\psi_{\mathbf{k}\tau b}\rangle = \epsilon_{\mathbf{k}\tau b} |\psi_{\mathbf{k}\tau b}\rangle \quad (\text{A10})$$

where $\tau \in \{K, K'\}$ and b labels bands. We will often use $\hat{\mathbf{c}}_{\mathbf{k}}^\dagger$ as a vector in (band, valley) for concision. As mentioned in the main text we consider an interacting Hamiltonian

$$\hat{H} = -\hat{h} + \frac{1}{2A} \sum_{\mathbf{q}} V_{\mathbf{q}} : \hat{\rho}_{\mathbf{q}} \hat{\rho}_{-\mathbf{q}} :, \quad V_{\mathbf{q}} = \frac{2\pi \tanh(qd)}{\epsilon_r \epsilon_0 q}, \quad (\text{A11})$$

where

$$\hat{\rho}_{\mathbf{q}} = \sum_{\mathbf{k}} \hat{\mathbf{c}}_{\mathbf{k}}^\dagger \Lambda_{\mathbf{q}}(\mathbf{k}) \hat{\mathbf{c}}_{\mathbf{k}}; \quad \Lambda_{\mathbf{q}}(\mathbf{k}) = \langle u_{\mathbf{k}} | u_{\mathbf{k}+\mathbf{q}} \rangle \quad (\text{A12})$$

is the density operator, A is sample area, normal ordering is relative to filling $\nu = 0$, and $\epsilon_r \approx 5 - 15$ is the dielectric constant. As usual, $V_{\mathbf{q}}$ corresponds to double-gate screened Coulomb interactions with gates at distance $d = 100 \text{ \AA}$ to 300 \AA . Here interactions are added directly to the “bare” kinetic term $\hat{h} = \sum_{\mathbf{k}} \sum_{\tau \in \{K, K'\}} \hat{\mathbf{c}}_{\mathbf{k}\tau}^\dagger h_\tau(\mathbf{k}) \hat{\mathbf{c}}_{\mathbf{k}\tau}$, where h_K , Eq. (A5), is determined by, e.g., first principles calculations of the insulating state where the chemical potential is inside the large valence-conduction gap. This is markedly different from interacting gapless systems like twisted bilayer graphene where the single-particle Hamiltonian is quite different from the bare Hamiltonian, and one must apply “Hartree-Fock subtraction” [104, 108] or other renormalization procedures [109] to determine the bare kinetic term. Furthermore, in this situation, integrating out all but the top few valence bands at mean-field level is equivalent to *projecting* to those top few bands; we may form a low-energy effective model of the top valence band by simply restricting the sum over bands in Eqs. (A11), (A12).

Self-Consistent Hartree-Fock In the main text and Fig. 1 we make use of standard self-consistent Hartree-Fock (SCHF) calculations. We briefly detail them here for completeness. Consider a single-particle density matrix $P(\mathbf{k})_{ab} = \langle c_{kb} c_{ka}^\dagger \rangle$. Such density matrices are bijective to Slater determinant states. As usual, we define Hartree and Fock Hamiltonians

$$h_H[P](\mathbf{k}) = \frac{1}{A} \sum_{\mathbf{g}} V_{\mathbf{g}} \Lambda_{\mathbf{g}}(\mathbf{k}) \sum_{\mathbf{k}} \text{tr}[P(\mathbf{k}) \Lambda_{\mathbf{g}}^\dagger(\mathbf{k})] \quad (\text{A13a})$$

$$h_F[P](\mathbf{k}) = -\frac{1}{A} \sum_{\mathbf{q}} V_{\mathbf{q}} \Lambda_{\mathbf{q}}(\mathbf{k}) P([\mathbf{k} + \mathbf{q}]) \Lambda_{\mathbf{q}}(\mathbf{k})^\dagger. \quad (\text{A13b})$$

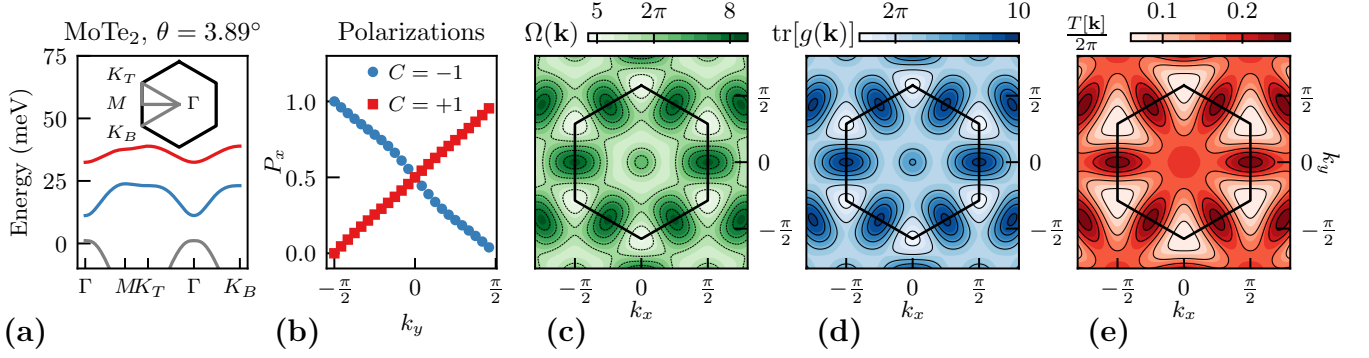


FIG. 5. (a) Band structure of twisted MoTe₂ material at parameter $\theta = 3.89^\circ$. The red band and blue bands are the top-most two hole bands. (b) Wilson line of the top-most two hole bands demonstrating they carry Chern number $C = -1$ and $C = +1$, respectively. (c) to (e): the momentum space quantum geometric properties of the top-most band (red), where (c) is the Berry curvature, (d) computes the trace of Fubini-Study metric and (e) depicts the deviation of trace condition in the Brillouin zone.

Here form factors $\Lambda_{\mathbf{q}}(\mathbf{k})$ are matrices in (band, valley) space. In terms of these, the energy of a Slater determinant state has energy $E[P] = \langle \hat{H} \rangle_P = \frac{1}{2} \text{Tr}[P(h + h_H[P] + h_F[P])]$ where h is the single-particle Hamiltonian and Tr is the trace over both \mathbf{k} and bands. If the self-consistency condition $[P, h_{HF}[P]] = 0$ is satisfied for all \mathbf{k} , then $E[P]$ is a local minimum. In practice we consider the top four valence bands of both valleys on a k -grid of size 24×24 , and use the standard “ODA” algorithm to achieve the self-consistency condition at $\nu = -1$ to numerical precision, imposing valley polarization and C_3 symmetry. Fig. 1 shows the resulting SCHF bandstructure along high-symmetry lines.

Appendix B: Quantum Geometry

In this section we review momentum-space band geometry [42] and its relationship to the real-space vortexability criterion [75]. We begin by introducing

$$\eta^{\mu\nu}(\mathbf{k}) = \sum_a \langle \partial_{k_\mu} u_{\mathbf{k}a} | Q(\mathbf{k}) | \partial_{k_\nu} u_{\mathbf{k}a} \rangle, \quad (\text{B1})$$

$$Q(\mathbf{k}) = 1 - \sum_a |u_{\mathbf{k}a}\rangle \langle u_{\mathbf{k}a}|; \quad P = \sum_{\mathbf{k}, a} |\psi_{\mathbf{k}a}\rangle \langle \psi_{\mathbf{k}a}|, \quad (\text{B2})$$

where $\eta^{\mu\nu}$ is the so-called quantum geometric tensor. The real and imaginary part of the quantum geometric tensor defines the Fubini-Study metric and Berry curvature, respectively:

$$g^{\mu\nu}(\mathbf{k}) = \text{Re}(\eta^{\mu\nu}), \quad \Omega(\mathbf{k})\epsilon^{\mu\nu} = -\frac{1}{2}\text{Im}(\eta^{\mu\nu}). \quad (\text{B3})$$

The metric $g^{\mu\nu}$ and the Berry curvature two form $\Omega(\mathbf{k})\epsilon^{\mu\nu}$ assign the Brillouin zone a Riemann structure and symplectic structure, respectively. When these two structures are “compatible”, holomorphic coordinates can be defined [70–72].

A sufficient compatibility condition is given by $\text{Tr} g(\mathbf{k}) = \Omega(\mathbf{k})$, which we focus on here, though we briefly comment on possible generalizations. Refs. [70–72] discuss the most general momentum-space compatibility condition (the so-called “determinant condition” [42, 67]. Ref. [73] focuses a sub-class related to the trace condition by linear transformations; only this sub-class implies real-space vortexability, and an orthogonal argument based on “forgetting translation symmetry” further distinguishes this class [75]. Vortexability may also be related to a Kähler geometry in real-space, and different choices of vortex functions $z \neq x + iy$ correspond to a wide variety of different real-space Kähler structures, most of which do not correspond to ideal momentum space geometry in the traditional sense [75].

The following conditions are equivalent conditions [70–73, 75]:

1. Trace Condition: $\text{Tr} g(\mathbf{k}) = \Omega(\mathbf{k})$, for all momentum \mathbf{k} in the first Brillouin zone. This condition is equivalent to the saturation of the general trace inequality: $\text{Tr} g(\mathbf{k}) \geq \Omega(\mathbf{k})$.
2. Momentum Space Holomorphicity: $Q(\mathbf{k}) |\bar{\partial}_k u_{\mathbf{k}a}\rangle = 0$, where $\bar{\partial}_k = \partial_{k_x} + i\partial_{k_y}$, for all momentum \mathbf{k} in the first Brillouin zone. This condition is equivalent to the existence of an unnormalized gauge in momentum space for the Bloch wavefunctions $|u_{\mathbf{k}a}\rangle$ such that $u_{\mathbf{k}a}$ is holomorphic in $k_x + ik_y$.
3. Vortexability: $\hat{z}\psi = P\hat{z}\psi$, where $z = x + iy$, for all states ψ belonging to the bands in the projector P . This condition is equivalent to the one used in text $\hat{z}P = P\hat{z}P$.

In Fig. 5(c, d, e) we show the quantum geometry of the top-most valence band. Particularly, it almost saturates the trace bound $T = \int d^2\mathbf{k} (\text{Tr} g(\mathbf{k}) - \Omega(\mathbf{k})) \geq 0$.

The momentum space holomorphicity condition is extremely powerful for constraining the form of flat band

wavefunctions, and has been used to prove the generality of the wavefunctions (3) for single $C = 1$ bands and related results for single bands with $C > 1$ [73, 76, 77].

We now outline how to derive the circular dichroism result Eq. (5). Consider a band with projector $P = \sum_{\mathbf{k}, b} |\psi_{\mathbf{k}b}\rangle \langle \psi_{\mathbf{k}b}|$ and $Q = I - P$. Using the vortexability condition of $\hat{z}P = P\hat{z}P$, we see that $Q\hat{z}P = 0$; thus, taking the Hermitian conjugate, $P\hat{z}^\dagger Q = 0$. In that case, $0 = \|P\hat{z}^\dagger Q\| = \sum_{a \in P, b \in Q} \sum_{\mathbf{k}} |\langle \psi_{\mathbf{k}a} | \hat{z}^\dagger | \psi_{\mathbf{k}b} \rangle|^2$ so $\langle \psi_{\mathbf{k}a} | \hat{z}^\dagger | \psi_{\mathbf{k}b} \rangle = 0$ since each term is positive. Now consider matrix elements $v_{ab}^- = \langle \psi_{\mathbf{k}a} | \hat{v}^- | \psi_{\mathbf{k}b} \rangle = -i \langle \psi_{\mathbf{k}a} | [\hat{z}^\dagger, \hat{H}] | \psi_{\mathbf{k}b} \rangle$. Since each both $|\psi_{\mathbf{k}a}\rangle$ and $|\psi_{\mathbf{k}b}\rangle$ are eigenstates, we derive that

$$v_{ab}^- = -i(\epsilon_{\mathbf{k}b} - \epsilon_{\mathbf{k}a}) \langle \psi_{\mathbf{k}a} | \hat{z}^\dagger | \psi_{\mathbf{k}b} \rangle = 0 \quad (\text{B4})$$

Consider the definition of the optical response which we reproduce below:

$$\sigma_{Q \rightarrow P}^\pm(\omega) = \frac{ie^2}{\hbar} \sum_{\mathbf{k}, a \in Q, b \in P} \frac{f_{ab} |\langle \psi_{\mathbf{k}a} | \hat{v}^\pm | \psi_{\mathbf{k}b} \rangle|^2}{\epsilon_{ab} \omega - \epsilon_{ab}}. \quad (\text{B5})$$

If the chemical potential is placed such that some of the states corresponding to Q are filled and P is unfilled, then the right handed optical transitions corresponding to $Q \rightarrow P$ will be extinguished: $\sigma_{Q \rightarrow P}^-(\omega) = 0$ uniformly, whereas σ^+ is generically non-zero.

Appendix C: Exact Diagonalization

We perform exact diagonalization of the model (1) at different system sizes. At half filling $\nu = -1/2$, we point out that the CFL phase can be realized in a large portion in the phase diagram (V, ϵ_r, θ) of twisted TMD. In particular, Fig. 6 lists spectra of moiré TMD at $(V, \epsilon_r, \theta) = (0, 8.0, 3.89^\circ)$ for various system sizes, and compares them to the spectra of Coulomb interaction in LLL of the same system sizes. The similarities between the spectra of twisted TMD and LLL strongly suggest the interacting low energy states in TMD are CFLs, because Coulomb interaction is known to stabilize the CFL phase in LLL [110]. Moreover, for each system size, the momentum of low energy many-body eigenstates agree with the total momentum of compact composite Fermi seas, again indicating the phase is a CFL [81]. We further confirm the CFL phase by computing the electron occupation $n(\mathbf{k})$ in the Brillouin zone and show that it's featureless in the CFL phase but shows a Fermi surface in the FL phase. The CFL phase region is centered around $\theta \approx 3.6^\circ$, $V = 0$ and small ϵ_r , as expected due to a compromise between the $\nu = -1, 0$ parent-state bandwidths. Finally, we comment on the possibility to see a CFL at $\nu = -3/4$.

1. Low energy spectrum and the identification of emergent Fermi sea

The similarities between the spectrum of LLL and moiré TMD, shown in Fig. 6, strongly suggest the ground states of twisted TMD are CFLs. Here we analyze the ED spectrum in more detail and explain why they point to the emergent Fermi sea.

To compare the spectrum between LLL and moiré TMD, we adopt the same real space geometry on these two systems. The vectors that generate the $N_1 \times N_2$ torus are $\mathbf{L}_i = N_i \mathbf{a}_i$, written in terms of the lattice vectors \mathbf{a}_1 and \mathbf{a}_2 . We define the corresponding reciprocal lattice vectors as \mathbf{b}_1 and \mathbf{b}_2 in which $\mathbf{a}_i \cdot \mathbf{b}_j = 2\pi \delta_{ij}$. Since we have chosen identical geometries for these two systems, we can also choose $\mathbf{a}_{1,2}$ to denote the basis vectors for the magnetic unit cell in LLL as well as the basis vectors for unit cell in moiré TMDs. We start by reviewing translation symmetries and features of the CFL spectrum in LLL; we will later find that similar discussions apply to moiré TMD straightforwardly. We choose the magnetic field such that there is one flux quantum per unit cell, so the number of fluxes $N_\phi = N_1 N_2$.

We first review the magnetic translation boundary conditions in LLL. Without loss of generality, we impose arbitrary twisted boundary conditions on our Hilbert space by threading fluxes ϕ_i through the non-contractible loops of the torus generated by \mathbf{L}_i . This choice of boundary conditions then defines the single particle Hilbert space, in which every state satisfies the relation [111, 112]

$$T_{\mathbf{L}_i}^{\text{mag}} \psi = (-1)^{N_\phi} e^{i\phi_i} \psi. \quad (\text{C1})$$

We emphasize that making a choice of boundary conditions breaks the continuous magnetic translation symmetry of the LLL, and generally applying an arbitrary magnetic translation to each electron in the state will change the boundary condition [111–113]. We can use this property to relate states with different ϕ_i to each other.

We then define boundary conditions for composite fermions. To analyze composite fermion boundary conditions we must choose a trial wavefunction to begin with. We choose the widely accepted Read-Rezayi wavefunction, reproduced below [95]:

$$\Psi(\{\mathbf{r}_n\}) = \mathcal{P}_{\text{LLL}} \det_{mn} \left(e^{i\tilde{\mathbf{k}}_m \cdot \mathbf{r}_n} \right) \Psi_L(\{\mathbf{r}_n\}) \quad (\text{C2})$$

This wavefunction can be understood from a parton construction similar to the one in the main text. The first term, $\Psi_f = \det \left(e^{i\tilde{\mathbf{k}}_m \cdot \mathbf{r}_n} \right)$, describes a composite Fermi sea of fermions that feel no flux. The second term $\Psi_L(\{\mathbf{r}_n\})$ describes a bosonic Laughlin state of bosons that do feel the electronic flux. We will see that the composite fermion boundary conditions, manifesting through the quantization of the CF momenta $\tilde{\mathbf{k}}_m$, can be completely different than the electron boundary conditions. This is because the CFs boundary condition is set by the

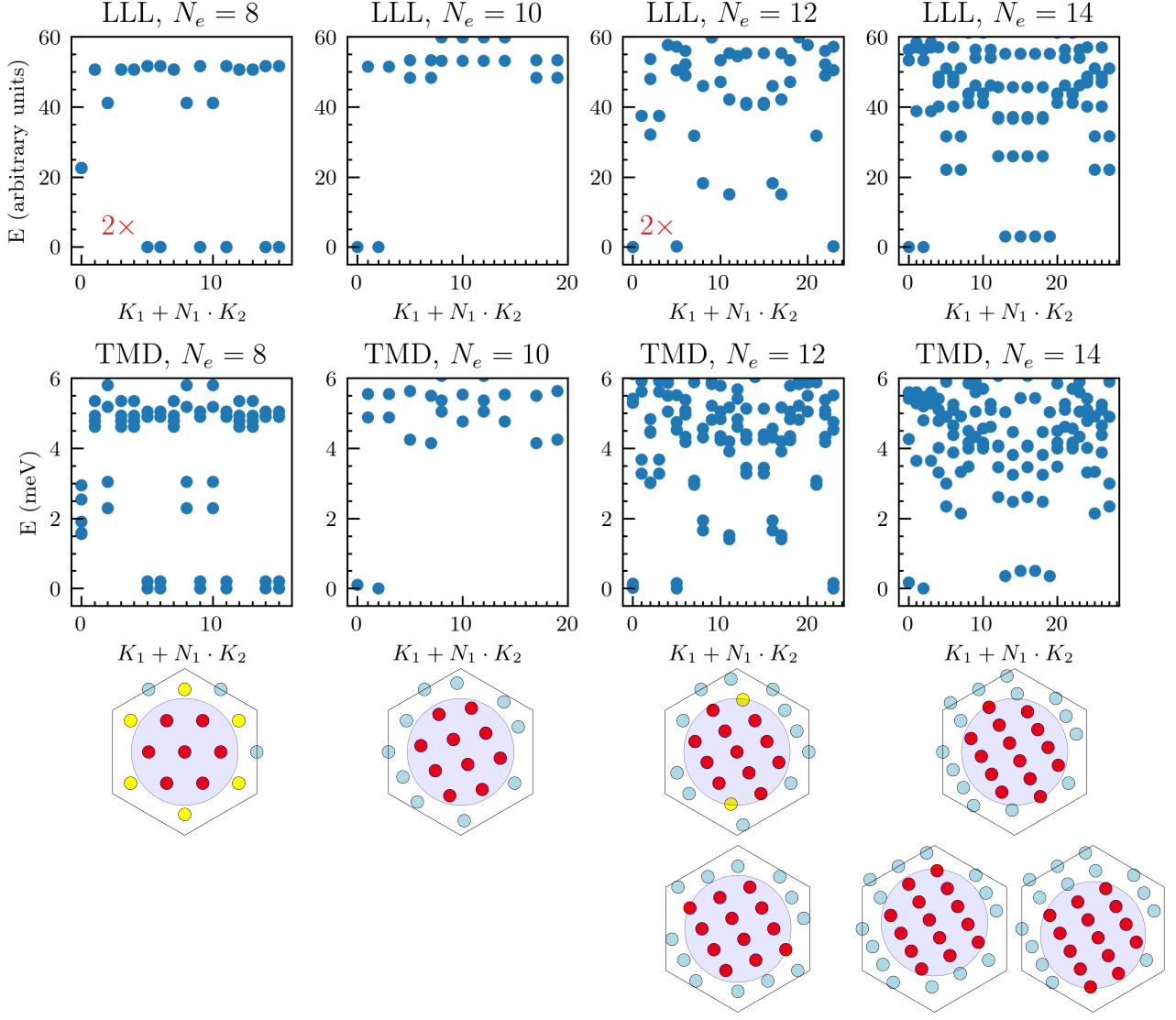


FIG. 6. Comparison between the spectrum of half filled LLL with Coulomb interaction (top row) and that of twisted MoTe₂ (middle row) for different system sizes at $(V, \epsilon_r, \theta) = (0, 8, 3.89^\circ)$. The third and fourth row illustrate the composite fermion configuration for the low energy states. We note each point in the spectrum shown in the LLL in $N_e = 8$ and $N_e = 12$ are two fold degenerate, related to the continuous center of mass magnetic translation symmetry; the center of mass partner differs their momentum by $(\delta K_1, \delta K_2) = (2, 0)$ for $N_e = 10$ and $N_e = 14$.

emergent gauge flux through the torus handles, which is *dynamical*.

To impose the boundary conditions (C1), we note that individual magnetic translations $T_{j, \mathbf{L}_i}^{\text{mag}}$ commute with the projector to the LLL: $[T_{j, \mathbf{L}_i}^{\text{mag}}, \mathcal{P}_{\text{LLL}}] = 0$. We then apply the magnetic translation on the j th particle in (C2). By using the commutativity of magnetic translation and LLL projection we arrive at,

$$T_{j, \mathbf{L}_i}^{\text{mag}} \Psi = \mathcal{P}_{\text{LLL}} \left[(t_{j, \mathbf{L}_i} \Psi_f) \left(T_{j, \mathbf{L}_i}^{\text{mag}} \Psi_L \right) \right], \quad (\text{C3})$$

where t_{j, \mathbf{L}_i} is an ordinary translation, with no magnetic twist. Here we have placed the magnetic twist factor onto the translation of the Laughlin state, anticipating the fact

that the Laughlin state can be symmetric under magnetic translations while the zero-flux fermion wavefunction is symmetric under ordinary translations.

We suppose that the bosonic Laughlin wavefunctions satisfy boundary condition $\phi_i^{(b)}$, not necessarily equal to ϕ_i :

$$T_{j, \mathbf{L}_i}^{\text{mag}} \Psi_L = (-1)^{N_\phi} e^{i\phi_i^{(b)}} \Psi_L \quad (\text{C4})$$

Note that Laughlin states have a two-fold degeneracy due to the part of the center of mass translation symmetry. This degeneracy directly translates to the center of mass degeneracy of the composite fermion wavefunction (C2).

We now impose boundary conditions on the composite

fermion part of the wavefunction

$$\begin{aligned} t_{j,\mathbf{L}_i}^{\text{mag}} \Psi_f &= \left(\sum_P (-1)^P e^{i\tilde{\mathbf{k}}_{P(j)} \cdot \mathbf{L}_i} e^{i\tilde{\mathbf{k}}_{P(m)} \cdot \mathbf{r}_n} \right) \\ &= e^{i\phi_i^{(f)}} \mathcal{P}_{\text{LLL}} \det_{mn} \left(e^{i\tilde{\mathbf{k}}_m \cdot \mathbf{r}_n} \right), \end{aligned} \quad (\text{C5})$$

which corresponds to $e^{i\mathbf{k}_j \cdot \mathbf{L}_i} = e^{i\phi_i^{(f)}}$. The quantization of composite fermion momentum is thus

$$\tilde{\mathbf{k}} = \frac{n_1 + \frac{\phi_1^{(f)}}{2\pi}}{N_1} \mathbf{b}_1 + \frac{n_2 + \frac{\phi_2^{(f)}}{2\pi}}{N_2} \mathbf{b}_2. \quad (\text{C6})$$

The boundary conditions of the two sub-wavefunctions then sum to the electron boundary conditions

$$\phi_i = \phi_i^{(f)} + \phi_i^{(b)}. \quad (\text{C7})$$

Indeed, the boundary condition for electrons — corresponding to the electromagnetic fluxes through the handles of the torus — are split up between the CFs and the composite bosons that form the Laughlin state. The “relative” degree of freedom, corresponding to increasing $\phi_i^{(f)}$ while decreasing $\phi_i^{(b)}$, such that ϕ_i is held fixed, corresponds to the dynamical flux of the emergent gauge field.

We now compute the center of mass momentum for the state (C2). To do this, we define the center of mass momentum \mathbf{K} for a state as

$$\left(\prod_j T_{j,\mathbf{a}_i}^{\text{mag}} \right) \Psi = e^{i\mathbf{K} \cdot \mathbf{a}_i} \Psi. \quad (\text{C8})$$

This definition is such that there always exists a bosonic Laughlin state which, when periodic boundary condition $\phi_i^{(b)} = 0$ is imposed, has zero center of mass momentum $K_1 = K_2 = 0$.

Starting with this canonical definition of COM momentum at periodic boundary condition, the COM momentum at arbitrary boundary condition can be obtained from flux insertion:

$$\mathbf{K}(\phi) = N_e \left(\frac{\phi_1}{2\pi N_1} \mathbf{b}_1 + \frac{\phi_2}{2\pi N_2} \mathbf{b}_2 \right) + \mathbf{K}(\phi = 0). \quad (\text{C9})$$

Following (C8), we are ready to compute the center of mass momentum for the state (C2):

$$\begin{aligned} &\left(\prod_j T_{j,\mathbf{a}_i}^{\text{mag}} \right) \Psi(\{\mathbf{r}_n\}) \\ &= e^{i\sum_m \tilde{\mathbf{k}}_m \cdot \mathbf{a}_i} \mathcal{P}_{\text{LLL}} \det_{mn} \left(e^{i\tilde{\mathbf{k}}_m \cdot \mathbf{r}_n} \right) \left(\prod_j T_{j,\mathbf{a}_i}^{\text{mag}} \right) \Psi_L(\{\mathbf{r}_n\}) \\ &= e^{i(\sum_m \tilde{\mathbf{k}}_m + \mathbf{K}_L(\phi^{(b)})) \cdot \mathbf{a}_i} \Psi(\{\mathbf{r}_n\}), \end{aligned} \quad (\text{C10})$$

from which the COM momentum can be read out as

$$\begin{aligned} \mathbf{K}_\Psi &= \sum_m \tilde{\mathbf{k}}_m + \mathbf{K}_L(\phi^{(b)}), \\ &= \sum_m \tilde{\mathbf{k}}_m + \frac{N_e \phi_1^{(b)}}{2\pi N_1} \mathbf{b}_1 + \frac{N_e \phi_2^{(b)}}{2\pi N_2} \mathbf{b}_2, \end{aligned} \quad (\text{C11})$$

where we have applied (C9) for the bosonic Laughlin state in the second line.

From (C11), (C6) and (C7), we notice that the COM momentum of the CFL state \mathbf{K}_Ψ is entirely determined by the physical boundary condition $\phi_{1,2}$ and the integer part of composite fermion momenta $\{\tilde{\mathbf{k}}_i\}$. This means that the COM momentum is determined by $\phi_{1,2}$ and the relative configuration of the composite fermion momenta. Thus, for the purpose of interpreting CFL many body momentum from ED numerics, the concrete value of $\phi_i^{(f)}$ does not matter.

However, there could be a preferred $\phi_i^{(f)}$ energetically. We assume that $\phi_i^{(f)}$ is self-consistently chosen for each state such that the compact composite Fermi sea is centered at Γ to minimize the variational energy, which we conjecture to be captured by a dispersion $E(\tilde{\mathbf{k}})$ that grows with $|\tilde{\mathbf{k}}|$ for the particle-hole symmetric CFL state in LLL. When we plot the composite Fermi sea in Fig. 6, we pick particular choices of $\phi_{1,2}^{(f)}$ for each system size such that the composite Fermi sea is centered at Γ .

We now describe the CFL COM momentum counting for all the low energy states in all system sizes. For all system sizes N_1, N_2 we study here, we can choose the physical boundary condition to be $\phi_i = 0$.

We start with $N_e = 8$ electrons on a 4×4 torus. In this case, $\phi_i^{(b)} = -\phi_i^{(f)} = 0$ already gives a composite fermion Fermi sea centered at Γ point. For both LLL and twisted TMD, there are 12 low energy states living in 6 momentum sectors consisting of the ground state manifold. These twelve states, six modulo center of mass degeneracy, correspond to the six possible momenta for the eighth, highest energy, composite fermion shown in yellow in the third row of Fig. 6.

We proceed and focus on $N_e = 10$ electrons on a 4×5 torus. We choose $\phi_2^{(b)} = -\phi_2^{(f)} = \pi$ to give a presumably low energy composite fermion configuration centered at Γ . From the configuration shown in the third row $\sum \tilde{\mathbf{k}}_i = 0$, $\mathbf{K} = N_e \phi_2^{(b)} / 2\pi N_2 \mathbf{b}_2 = \mathbf{b}_2$, which corresponds to the state appearing in sector 0. The state in sector 2 is related to this state by center of mass translation.

We then study $N_e = 12$ electrons on a 4×6 torus. We argue that two different boundary conditions must be chosen for the low energy states: $\phi_i^{(b)} = -\phi_i^{(f)} = 0$ for the states appearing in energy sectors 5 and 23, shown in the third row, and $\phi_2^{(b)} = -\phi_2^{(f)} = \pi$ which appears in sector 0, shown in the fourth row. We numerically observe these two ED states are close in energy.

We conclude by analyzing $N_e = 14$ electrons on a 4×7 torus. We choose $\phi_2^{(b)} = -\phi_2^{(f)} = \pi$. The symmetric

Fermi sea configuration shown in the third row corresponds to the states in sector 0, which is again related to the state in sector 2 by the center of mass magnetic translations. On the other hand, the other low energy states, corresponding to less symmetric composite fermion Fermi seas, are shown in the fourth row.

2. Explicitly LLL or ideal band projected CFL wavefunction

Here we comment that there exists an explicitly LLL projected CFL wavefunction defined on the torus geometry [81, 113–115], and such a wavefunction can be easily generalized to be an ansatz for the CFL state which is explicitly projected to ideal flatbands. In LLL, such projected wavefunction reads:

$$\begin{aligned}\Psi_{\text{CFL}} &= \det M_{ij} \prod_{k=1}^2 f\left(\sum_i z_i - \alpha_k\right). \quad (\text{C12}) \\ M_{ij} &= e^{\frac{1}{8}(z_i d_j^* - z_i^* d_j)} \prod_{k \neq i}^{N_e} f(z_i - z_k - d_j + \bar{d}), \\ d_i &= \frac{mL_1 + nL_2}{N_e} + \frac{L^{(f)}}{N_e}; \quad \sum_{k=1}^2 \alpha_k = L^{(b)},\end{aligned}$$

where d_i is the complex coordinate of the composite fermion dipole $d_i = d_i^x + id_i^y$, and $z = x + iy$ is the complex coordinate of electron. In LLL, the dipole is related to the momentum of composite fermion via dipole-momentum locking $d^a = 2l_B^2 \epsilon^{ab} \tilde{k}_b$. Since the reciprocal lattice is related by a 90° rotation and appropriate rescaling, $\mathbf{b}_i \rightarrow \epsilon_{ij} \mathbf{a}_j$, the dipole is quantized on a $L_{1,2}/N_e = 2L_{1,2}/(N_1 N_2)$ lattice and shifted by an internal flux $L^{(b/f)} = [-\phi_2^{(b/f)} L_1 + \phi_1^{(b/f)} L_2]/2\pi$. The \bar{d} is a parameter of the wavefunction and can be chosen as center of dipoles $\bar{d} = \sum_i d_i/N$. In the above $\alpha_{1,2}$ labels the COM zeros that determines the COM momentum of the bosonic Laughlin state, which is shifted by the Laughlin state's boundary condition. To obtain a torus wavefunction, we need to use Weierstrass sigma functions $\sigma(z)$ that is quasi-periodic in $L_{1,2}$, and we have defined $f(z) = \sigma(z) \exp(-|z|^2/4N_\phi)$ [113, 116, 117].

The link between the Read-Rezayi wavefunction (C2) and the projected wavefunction (C12) can be understood as follows. First, the Jastrow factor from the bosonic Laughlin wavefunction can be pulled into the determinant, so we can rewrite $\Psi_f \Psi_L$ as follows [118],

$$\left(\det_{ij} e^{i\mathbf{k}_j \cdot \mathbf{r}_i} \right) \prod_{i < j} (z_i - z_j)^2 = \det_{ij} \left[e^{i\mathbf{k}_j \cdot \mathbf{r}_i} \prod_{k \neq i} (z_i - z_k) \right].$$

Notice the Bloch factor $e^{i\mathbf{k} \cdot \mathbf{r}} = e^{i\mathbf{d} \times \mathbf{r}/2} = e^{(d\bar{z} - \bar{d}z)/4}$. We then approximate the LLL projection by replacing the anti-holomorphic coordinate \bar{z} with the holomorphic partial derivative $l_B^2 \partial_z$ such that $P_{\text{LLL}}(\Psi_f \Psi_L)$ is

approximated by $\det_{ij} \left(e^{\frac{1}{4} \bar{d}_j z_i} \prod_{k \neq i} (z_i - z_k - d_j) \right)$. Finally translating into torus geometry arrives at (C12). See Ref. [81] for details. Generalizing this wavefunction to $1/2m$ filling is straightforward [115].

In the end we comment that the exact mapping between LLL and ideal band mentioned in the main text, Eqn. (3), enables an explicit construction of CFL variational wavefunction without magnetic field: $\Psi_{\text{CFL}}^{\text{band}} = \Psi_{\text{CFL}}(\{z_i\}) \prod_i e^{-K(\mathbf{r}_i)} \zeta_i(\mathbf{r}_i)$. We leave a detailed study of this flat band CFL wavefunction for the future.

3. Phase Diagrams and Phase Identification

In this section, we discuss how to identify different phases from ED. We use multiple indicators, including:

- Momentum of low energy states.

In the previous section, we have discussed the momentum of low energy states from the CFL phase. They correspond precisely to the total momentum of composite fermions Fermi sea. Moreover, low energy states of CFL are nearly degenerate, corresponding to the exact COM degeneracy in LLL. For instance, for $N_e = 12$ particles, the low energy states of CFL has $K = K_1 + N_1 K_2 = 0, 5, 23$ and each of them are nearly two fold degenerate. Their composite Fermi sea configuration is plotted in Fig. 6.

Differently, Fermi liquids do not exhibit any signatures of COM degeneracy. See Fig. 7 for illustrations.

- The occupation number of ground state $n(\mathbf{k})$.

We can also identify the FL phase by computing the ground state occupation of momentum eigenstates in the Brillouin zone. In the CFL phase, the ground state occupations are relatively uniform throughout the Brillouin zone and there are no significant Fermi surface discontinuities in the occupation. On the other hand, in the FL phase, the ground state occupations not only exhibit a discontinuous feature at the putative Fermi surface, but also closely follow the non-interacting Fermi distribution $n_{(\epsilon, \mu)} = \theta(\epsilon - \mu)$ for holes very well, as shown in Fig. 8(b) and (c). The quasiparticle residue Z , which characterizes the discontinuity at the Fermi surface, is not 1 as the noninteracting FL because it is renormalized by the interactions. We note that this phase identifier is further supported by iDMRG results shown in Fig. 2(a), in which the CFL clearly shows a featureless Brillouin zone in terms of electron occupations, whereas the FL has a clear Fermi surface.

We cross-check the two methods by computing the zero displacement field phase diagram in the (θ, ϵ_r) plane, shown in Fig. 9. In this phase diagram, only the CFL

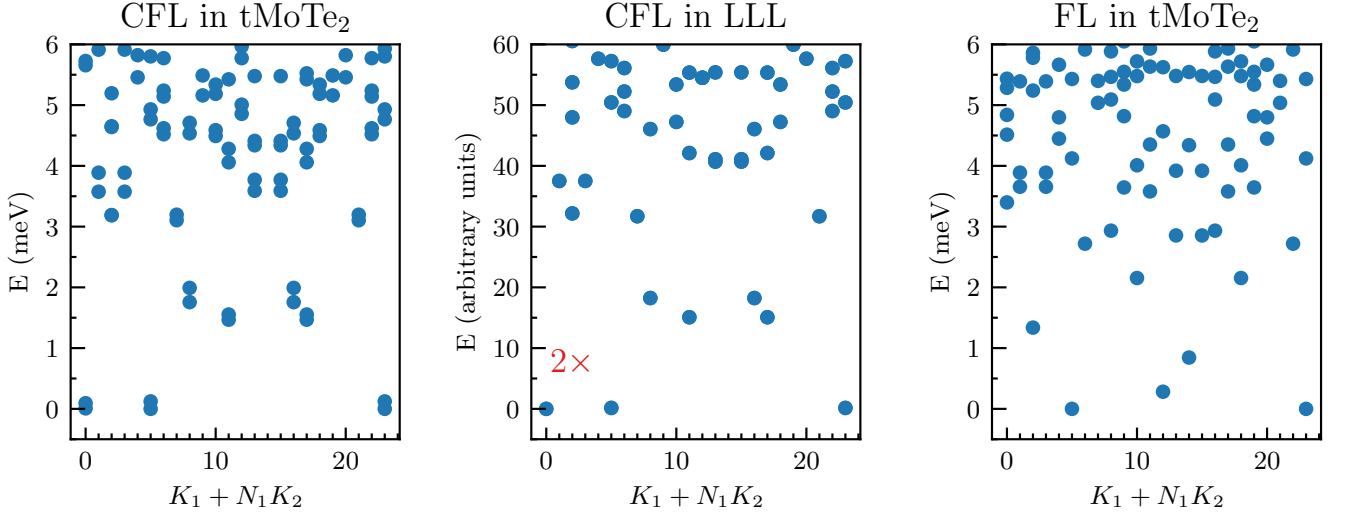


FIG. 7. Representative energy spectrum for the $\nu = -1/2$ CFL phase in twisted MoTe₂, the CFL phase in LLL, and the FL phase in twisted MoTe₂. All the ED are performed on 4×6 torus with the same geometry. Notably, for CFL phase the two-fold COM degeneracy is exact in LLL, whereas it is weakly broken in twisted MoTe₂. When the system transitions into the FL phase, the COM degeneracy is no longer present.

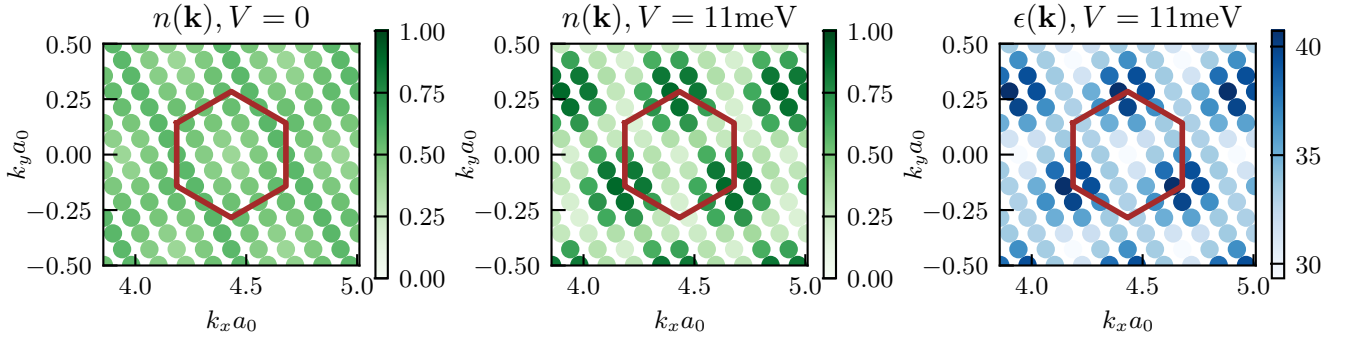


FIG. 8. Occupations of holes in the ED ground state in the CFL phase and the FL phase by tuning displacement field, respectively. All the ED are performed on 4 torus with the same geometry. The FL occupations match excellently to the Fermi distribution $\theta(\epsilon - \mu)$ for holes.

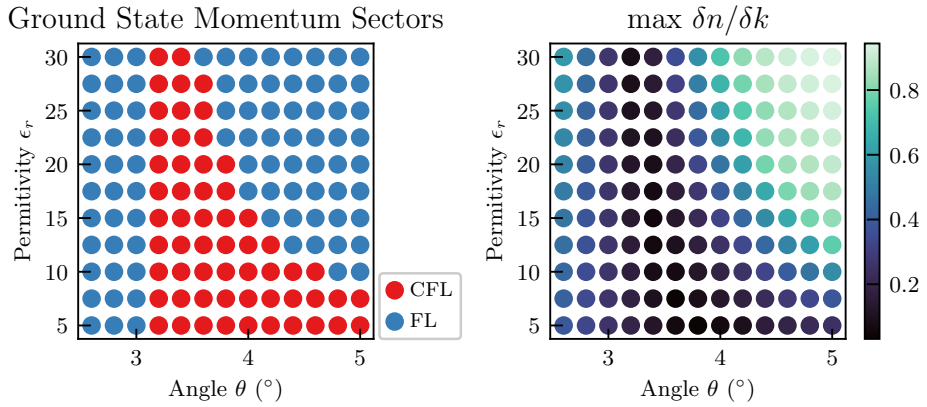


FIG. 9. Phase diagram of interacting twisted MoTe₂ at $\nu = -1/2$ at zero displacement field obtained from two different indicators from ED on a 4×6 torus. The phase diagram of left figure is resolved by the momentum structure of low energy states while that on the right is resolved from the occupation $\langle n(\mathbf{k}) \rangle$. See text for details.

and FL phases appear. The phase diagram computed by the low energy momentum sectors is shown in Fig. 9(a), in which the CFL phase is shown in red dots and the FL phase is shown in blue dots. The phase diagram computed by the finite differences in occupation is shown in Fig. 9(b). The dark regions represent a small variation in occupations and thus represent the CFL phase. The bright regions represent the FL phase. The shapes of the phase boundaries agree with each other.

In Fig. 3(b) we identify the phases in the (θ, V) plane using the many-body momentum sectors. We keep $\epsilon_r = 8$ throughout. There is clearly a large portion of the phase diagram exhibiting CFL-like features, represented by the red region centered around 3.6° with a small displacement from the CFL into the FL phase, shown in green.

We mark the topological transition line in gray and remark that near the topological phase transition the band gap closes so the band projection approximation in our ED procedure no longer works. We emphasize that this phase diagram is obtained assuming valley polarization throughout the parameters used in the phase diagram.

4. $\nu = -3/4$ Composite Fermi Liquid and Associated Phase Diagrams

The possibility of a $\nu = -3/4$ CFL is investigated also using ED on a 4×8 torus. Since such a state is closer to $\nu = -1$, we expect that it generally has a larger spin gap than the possible $\nu = -1/2$ CFL. This means that the valley polarization we assume in the ED procedure is better justified at this filling.

We compare the spectrum between the $\nu = -3/4$ CFL and the $\nu = 3/4$ CFL from the LLL using dual gate screened Coulomb interactions in Fig. 10. Each point in the LLL spectrum has a four fold center of mass degeneracy, which is weakly broken in twisted MoTe_2 . The similarity of the spectrum suggests that a CFL where 8π fluxes are attached to each electron can also be formed at $\nu = -3/4$.

In the last panel of Fig. 10 we show the many-body phase diagram at $\nu = -3/4$ assuming valley polarization. Since this filling is closer to $\nu = -1$ we conjecture that the valley polarization will be more stable to the displacement field. We see that the $\nu = -3/4$ CFL region (red) has significantly shrunk compared to the $\nu = -1/2$ CFL, and most of the phase diagram of the $C = 1$ band is a FL phase (green). We mark the topological transition line in black and remark that near the topological phase transition the band gap closes so the band projection approximation in our ED procedure is no longer valid (gray region).

Appendix D: Density Matrix Renormalization Group

This Appendix discusses the infinite density matrix renormalization group (iDMRG) numerics used in the main text. We first discuss the computational basis used, then express the structure factor in this basis, and finally give additional details on the phase identification including finite size scaling.

1. Computational Basis

For DMRG we consider a moiré lattice geometry

$$\mathbf{a}_1 = a_M \left(\frac{\sqrt{3}}{2}, \frac{1}{2} \right), \quad \mathbf{a}_2 = a_M (0, 1) \quad (\text{D1})$$

$$\mathbf{g}_1 = \frac{2\pi}{a_M} \left(\frac{2}{\sqrt{3}}, 0 \right), \quad \mathbf{g}_2 = \frac{2\pi}{a_M} \left(-\frac{1}{\sqrt{3}}, 1 \right). \quad (\text{D2})$$

where $a_M = |\mathbf{a}_1|$ is the moiré length. We consider rectangular Brillouin zone $\mathcal{B} = [-G_x/2, G_x/2] \times [-G_y/2, G_y/2]$ where $G_x = \frac{4\pi}{\sqrt{3}a}$, $G_y = \frac{2\pi}{a}$ so that $\mathbf{a}_1 = 2\pi \left(\frac{1}{G_x}, \frac{1}{2G_y} \right)$.

We solve the kinetic Hamiltonian Eq. (A5) as

$$h |\phi^{\mathbf{k}a}\rangle = \epsilon^{\mathbf{k}a} |\phi^{\mathbf{k}a}\rangle, \quad (\text{D3})$$

where $\ell = B, T = -1, +1$ labels layers, and a labels bands. We impose boundary conditions in the y direction corresponding to the momenta discretization

$$k_y[n] = G_y \begin{cases} -\frac{1}{2} + \frac{n + \frac{\Phi_y}{2\pi}}{L_x} & \text{if } L_y \equiv 0 \pmod{2} \\ -\frac{1}{2} + \frac{n + \frac{\Phi_y}{2\pi} + \frac{1}{2}}{L_x} & \text{if } L_y \equiv 1 \pmod{2} \end{cases}. \quad (\text{D4})$$

We therefore have L_y evenly ‘‘wires’’ across the Brillouin zone. The value of $L_x \gg 1$ does not affect the physics, provided that it is sufficiently long. If the external flux $\Phi_y = 0$, then one wire will go through Γ , giving periodic boundary conditions (PBC); $\Phi_y = 1/2$ corresponds to anti-periodic boundary conditions (APBC).

Following previous DMRG work on moiré systems [84, 104, 119, 120], we take a computational basis of hybrid Wannier functions that are maximally (exponentially) localized along \mathbf{a}_1 and periodic along $\mathbf{a}_2 \propto \hat{y}$. Let \hat{P} be a projector to the band (or bands) of interest. We transform to the Wannier-Qi states [82]

$$|w^{n, k_y, b}\rangle = \frac{1}{\sqrt{L_x}} \sum_{k_x} |\varphi^{\mathbf{k}b}\rangle e^{-i\mathbf{k} \cdot \mathbf{a}_1 n}, \quad |\varphi^{\mathbf{k}b}\rangle = |\phi^{\mathbf{k}a}\rangle U^{ab}(\mathbf{k}) \quad (\text{D5})$$

where $U_{nb}(\mathbf{k})$ is a unitary matrix that transforms into a Wannier gauge such that

$$\hat{T}_1 |w^{n, k_y, b}\rangle = |w^{n-1, k_y, b}\rangle \quad (\text{D6a})$$

$$\hat{T}_2 |w^{n, k_y, b}\rangle = e^{i2\pi k_y / G_y} |w^{n, k_y, b}\rangle \quad (\text{D6b})$$

$$\hat{P} e^{-i\hat{x}G_x} \hat{P} |w^{n, k_y, b}\rangle = e^{i2\pi[n + P_x(k_y, b)]} |w^{n, k_y, b}\rangle \quad (\text{D6c})$$

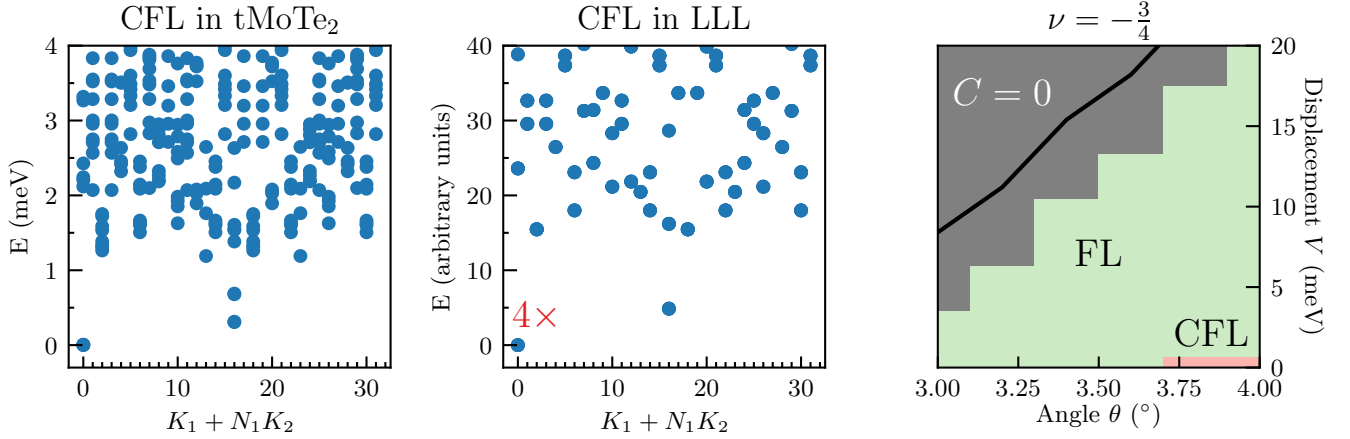


FIG. 10. Comparison between the spectrum of twisted MoTe₂ and the LLL at $\nu = -3/4$. The four fold center of mass degeneracy is broken weakly in twisted MoTe₂, but is too close to be resolved by eye in the ground state. We plot the phase diagram at $\epsilon_r = 8$ and $\nu = -3/4$. The large extent of the composite Fermi liquid phase is shown in red. The green regions correspond to Fermi liquid states, and the gray regions are near or past the $C = 1 \rightarrow 0$ topological transition marked with a black line. The composite Fermi liquid state is much more unstable to displacement field at $\nu = -3/4$ compared to $\nu = -1/2$.

where the polarizations $P_x(k_y, b) = \frac{G_x}{2\pi} \langle w^{0,k_y,b} | \hat{x} | w^{0,k_y,b} \rangle$ are the centers of the Wannier orbitals in the first unit cell, in accordance with the modern theory of polarization [121]. The polarizations for the top two valence bands of the K -valley are shown in Fig. 5(b). These have winding $C = \int dk_y \frac{dP_x}{dk_y} = +1, -1$ for the respectively, matching the Chern number [121]. We now specialize to the case where \hat{P} projects to the top $C = +1$ valence band of the K -valley (though this method applies equally well to both valleys and multiple bands, which will be the subject of future work).

At the many-body level, we consider Fermi creation operators

$$|\varphi^{\mathbf{k}}\rangle = \hat{c}_{\mathbf{k}}^\dagger |0\rangle, \quad \hat{c}_{\mathbf{k}}^\dagger = \frac{1}{\sqrt{L_x}} \sum_n e^{i\mathbf{k}\cdot\mathbf{a}_1 n} \hat{d}_{n,k_y}^\dagger, \quad (\text{D7})$$

which correspond to Bloch states and Wannier-Qi states in the top valence valence band of the K valley, respectively. We then express the Hamiltonian Eq. (A11) in the \hat{d}_{n,k_y}^\dagger basis, which should be interpreted as the putting the TMD Hamiltonian onto a cylinder geometry that is infinite along the x direction and periodic along the y direction with circumference L_y . The choice of maximally-localized Wannier orbitals along x ensures that hoppings decay as fast as possible in the x -direction. However, the quasi-long range screened Coulomb interactions decay quite slowly along x .

To perform infinite DMRG, one must express the Hamiltonian as a matrix product operator (see e.g. [122]), which is a tensor network composed of $2 \times 2 \times D \times D$ tensors where 2 is the physical dimension (for fermions) and D is the virtual “bond dimension”. One may naively construct an MPO from a Hamiltonian in the \hat{d}_{n,k_y}^\dagger basis by imposing a finite cutoff $M > 0$ on the interaction

range along the cylinder. However, this has two serious drawbacks: (i) the MPO bond dimension increases as $O(M^2)$, reaching $D \sim 2000$ by $M = 2$ at $L_y = 6$ [84] and (ii) the relative stability of various many-body ground states (particular quantum Hall states) are known to be sharply modified by the interaction distance. To circumvent this issue, some of us developed a technique of “MPO Compression” [83, 84], which creates a faithful representation of the MPO, including its quasi-long range interactions. In practice we ensure that the error of each matrix element of the Hamiltonian is $< 10^{-3}$ meV for up to 200 sites along the 1D chain. This technique has been previously applied to twisted bilayer graphene in the cases of 1, 2, 4, or 8 degrees of freedom per k -point [84, 104, 119, 120]. In this single-DOF case, the resulting bond dimensions are $D \sim 130 - 250$ for $L_y = 5 - 10$ respectively.

2. Structure Factor

To identify a composite Fermi liquid, we compute the structure factor, i.e. the density-density correlation function. The standard structure factor is defined as

$$S_0(\mathbf{q}) = \langle \hat{\rho}_{\mathbf{q}} \hat{\rho}_{-\mathbf{q}} \rangle \quad (\text{D8})$$

in terms of the density operator (A12). However, the dominant features of $S(\mathbf{q})$ here — and in any lattice system — are peaks at the Bragg lattice from $\langle \hat{\rho}_{\mathbf{q}} \rangle = \sum_{\mathbf{G}} \delta_{\mathbf{G}\mathbf{q}} \langle \hat{\rho}_{\mathbf{G}} \rangle$, where \mathbf{G} is a reciprocal lattice vector. To identify the non-trivial features associated to a (composite) Fermi surface, we focus on the connected part of the structure factor

$$S(\mathbf{q}) = \langle \hat{\rho}_{\mathbf{q}} \hat{\rho}_{-\mathbf{q}} \rangle - \langle \hat{\rho}_{\mathbf{q}} \rangle \langle \hat{\rho}_{-\mathbf{q}} \rangle. \quad (\text{D9})$$

We now resolve this in the computational basis \hat{d}_{n,k_y} . A straightforward, albeit lengthy, computation shows

$$S(\mathbf{q}) = \sum_{\substack{n_0 \in \mathbb{Z} \\ |\Delta N| \leq M \\ |\Delta n|, |\Delta n'| \leq N}} \sum_{k_y, k'_y} e^{i\mathbf{q} \cdot \mathbf{a}_1 (\Delta N + \Delta n' - \Delta n)} \tilde{\Lambda}_{\mathbf{q}}(\Delta n, k_y), \tilde{\Lambda}_{-\mathbf{q}}(\Delta n', k'_y) M_{\Delta n, k_y, \Delta n', k'_y, \Delta N, q_y} \quad (\text{D10a})$$

$$\tilde{\Lambda}_{\mathbf{q}}(\Delta n, k_y) = \sum_{k_x} e^{-i\mathbf{k} \cdot \mathbf{a}_1 \Delta n} \Lambda_{\mathbf{q}}(k_x, k_y) \quad (\text{D10b})$$

$$M_{\Delta n, k_y, \Delta n', k'_y, \Delta N, q_y} = \langle \hat{d}_{n_0, k_y}^\dagger \hat{d}_{n_0 + \Delta n, [k_y + q_y]} \hat{d}_{n_0 + \Delta N, k'_y}^\dagger \hat{d}_{n_0 + \Delta N + \Delta n', [k_y - q_y]} \rangle - \langle \hat{d}_{n_0, k_y}^\dagger \hat{d}_{n_0 + \Delta n, [k_y + q_y]} \rangle \langle \hat{d}_{n_0 + \Delta N, k'_y}^\dagger \hat{d}_{n_0 + \Delta N + \Delta n', [k_y - q_y]} \rangle. \quad (\text{D10c})$$

Here $[k_y + q_y]$ denotes that the quantity lies within the first Brillouin zone, and $M > 0$, $N > 0$ are finite-size cutoffs. As it is computationally expensive to compute $L_y^3(2M+1)(2N+1)^2$ observables in DMRG, we restrict to $N = 1$ (which is sufficient for small $|q_y| \lesssim G_y$), and take several hundred values of ΔN , q_x , which is sufficient to resolve fine features in Fourier space.

3. DMRG Phase Identification

This section details the phase identification of the Fermi liquid and composite Fermi liquid in DMRG. We focus on system sizes $L_y = 5, 8, 10$ and bond dimensions $\chi = 1024 - 4096$, which are sufficiently large to determine the phase unambiguously and converge most observables to high precision. To ensure that we only study differences in interacting physics, we study two representative states at $\nu = -1/2$ with (I) strong interactions $\epsilon_r = 6$ and (II) weak interactions $\epsilon_r = 60$ at $\theta = 3.89^\circ$.

We begin by examining the occupations $n(\mathbf{k}) = \langle \hat{c}_{\mathbf{k}}^\dagger \hat{c}_{\mathbf{k}} \rangle$ across the Brillouin zone. These are shown in Fig. 2(a) of the main text. For $\epsilon_r = 6$, the occupations are almost uniform, while for $\epsilon_r = 60$, the occupations are highly non-uniform with a sharp jump emerging as bond dimension increases. This behavior is characteristic of a Fermi liquid in cylinder DMRG: since the system is quasi-1D, no true Fermi liquid with quasiparticle weight $Z > 0$ can emerge. Instead, the ground state here is converging to (coupled) Luttinger liquids with a non-analyticity at the Fermi surface [123]. The locations of these features for the weakly-interacting state form an almost-circular Fermi surface centered at Γ — precisely what is expected for the weakly interacting Fermi liquid, given that the top band has a minimum at Γ . So far we have established that the weakly interacting state is highly consistent with a Fermi liquid, but the uniform occupations of the strongly-interacting state are consistent with both trivial insulators or more exotic possibilities.

We now examine entanglement scaling and correlation

lengths. Fig. 11(a,d) shows the scaling of entanglement entropy as a function of bond dimension. We see that both the weakly and strongly interacting states are highly entangled, consistent with a gapless state. To determine the character of potential gapless modes, we examine the spectrum of the transfer matrix. For a Fermi liquid, where adding an electron, hole, or particle-hole pair are all gapless excitations, one expects electron-electron, hole-hole, and density-density correlations to all show power-law behavior, with a diverging correlation length. For $\epsilon_r = 60$, we indeed find diverging correlation lengths for the electric charge $Q_E = +1, -1, 0$ sectors for all k_y , shown in Fig. 11(b,c). We conclude that the weakly interacting state is indeed a Fermi liquid. For the strongly interacting state, we see a similar increase in $Q_E = 0$ correlations without any accompanying increase in $Q_E = \pm 1$ correlations, shown in Fig. 11(e,f). This is consistent with a state that has gapless charge neutral excitations, but no gapless electrons and holes.

To understand the character of the neutral degrees of freedom, we turn to the structure factor $S(\mathbf{q})$ described above. Fig. 12 details the structure factor for both the weakly- and strongly-interacting states. As the minimum resolution in q_x is set by the density-density correlation length, we focus on $L_y = 5$ so that we may identify peaks, inflection points, and other sharp features.

We now show that the structure factors $S(\mathbf{q})$ for both the weakly and strongly interacting states are consistent with an almost-circular Fermi surface. Explicitly, assume a Fermi surface (not necessarily of electrons) of half the Brillouin zone area, i.e. $k_F = \sqrt{A_{BZ}/2\pi}$. Examining the geometry, we see that four of the five wires intersect a putative Fermi surface. (The assumption that the momenta of the quasiparticles that make up the Fermi surface matches the momenta of the wires holds here, but not in general [62].) On this quasi-1D system, we expect features in $S(\mathbf{q})$ whenever particle-hole pairs

$$\hat{c}_{\mathbf{k}}^\dagger \hat{c}_{\mathbf{k}+\mathbf{q}} \subset \hat{\rho}_{\mathbf{q}}$$

have \mathbf{k} and $\mathbf{k} + \mathbf{q}$ at intersections between wires and the

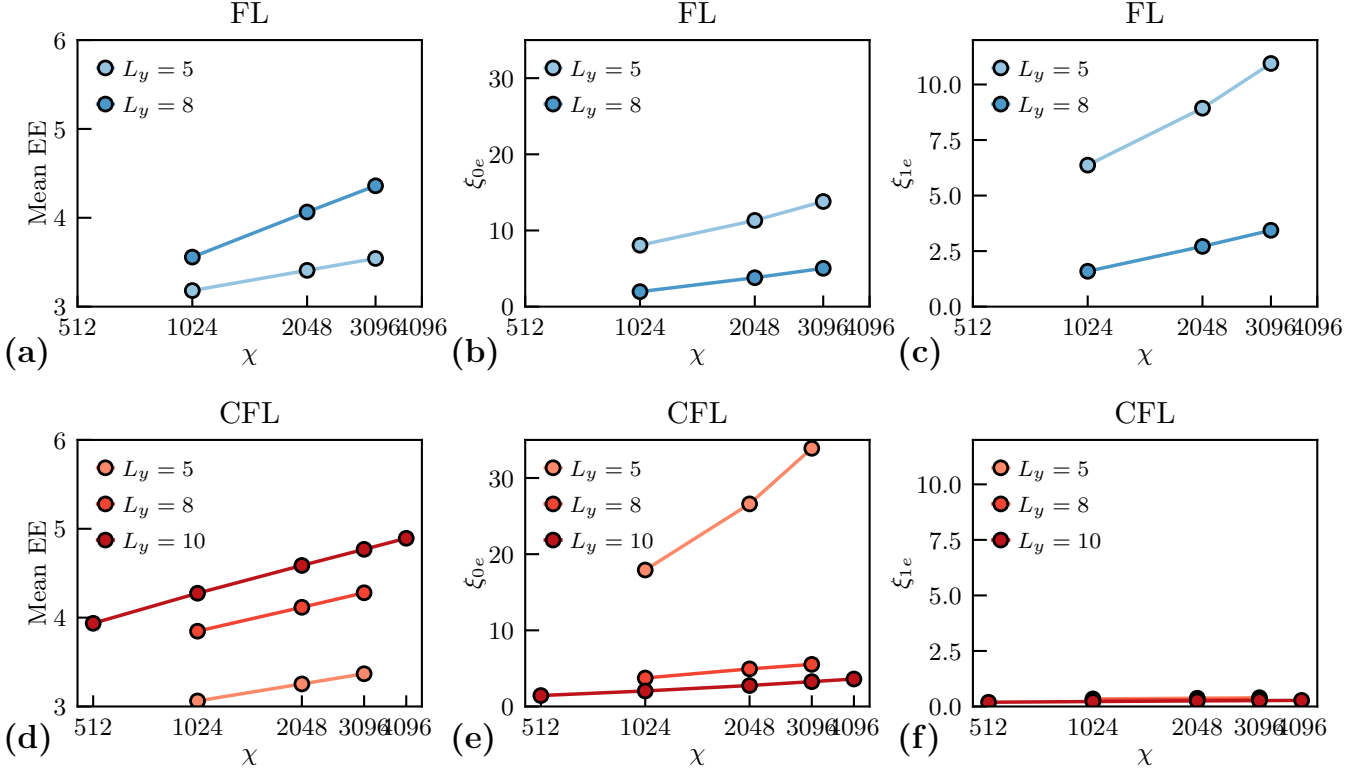


FIG. 11. Entanglement properties as a function of bond dimension χ . (a,d): the mean entanglement entropy measured. (b,e): the correlation length in the $Q_E = 0$ sector. The divergence in correlation length is consistent with the presences of gapless neutral excitations, corresponding to the particle-hole excitations in the Fermi liquid and density fluctuations in the composite Fermi liquid. (c,f): the correlation length in the $Q_E = 1$ sector. The Fermi liquid has a diverging correlation length, reflecting its gapless charged excitations – the electrons. In contrast, the composite Fermi liquid has small correlations in this sector.

Fermi surface. We label these intersections

$$\mathbf{k}_{A,B,C,D} = \left(-\sqrt{k_F^2 - k_y[n]^2}, k_y[n] \right), n = 1, 2, 3, 4,$$

on the left-hand side of the Fermi surface, and give corresponding labels $\mathbf{k}_{A',B',\dots}$ to the right-hand Fermi surface and higher Brillouin zones (see Fig. 12).

We identify features in $S(\mathbf{q})$ by taking its fractional derivative, defined through the Fourier transformations as follows:

$$\frac{d^\eta}{dq_x^\eta} S(q_x, q_y) = \int dx e^{-iq_x x} |x|^\eta \left(\int dq'_x e^{iq'_x x} S(q'_x, q_y) \right) \quad (\text{D11})$$

The fractional derivatives magnifies inflections and discontinuities in higher derivatives, making the scattering processes much more visible to the eye. We take various $\eta \in [1/3, 5/2]$ for display.

We observe that the FL structure factors show a much larger *umklapp* scattering than the structure factors of CFL in Fig. 12. The reason is that the Fermi liquid has a large density modulation in the unit cell, strongly enhancing the amplitude of *umklapp* scatterings, whereas the CFL has a much milder density modulation. We comment that enhancing the density modulation of the

CFL may enhance the *umklapp* scattering and introduce deformations of the composite Fermi surface [124].

Appendix E: More on experimental aspect of Chern band CFL

The CFL is a gapless, compressible phase and in the absence of a quantized response is more challenging to establish as compared to gapped FQHE states. Nevertheless, it has many striking physical responses which are distinct from that of other gapless phases, in particular the Fermi liquid (FL). The experimental signatures include transport properties, tunneling density of states and finite momentum conductivity.

A direct probe of the composite nature of the CFL quasiparticles is revealed in the tunneling density of states (tDOS). The tDOS for a Fermi liquid is finite even at zero bias, a consequence of the low energy electron like quasiparticles. However, physical electrons cannot be injected into a CFL at zero bias, leading to a “psuedogap” density of states. In particular the low energy tDOS of a CFL varies as $A(\omega) \propto e^{-\omega_0/\omega}$ as a function of bias ω [100]. The tDOS can be measured through the tunneling

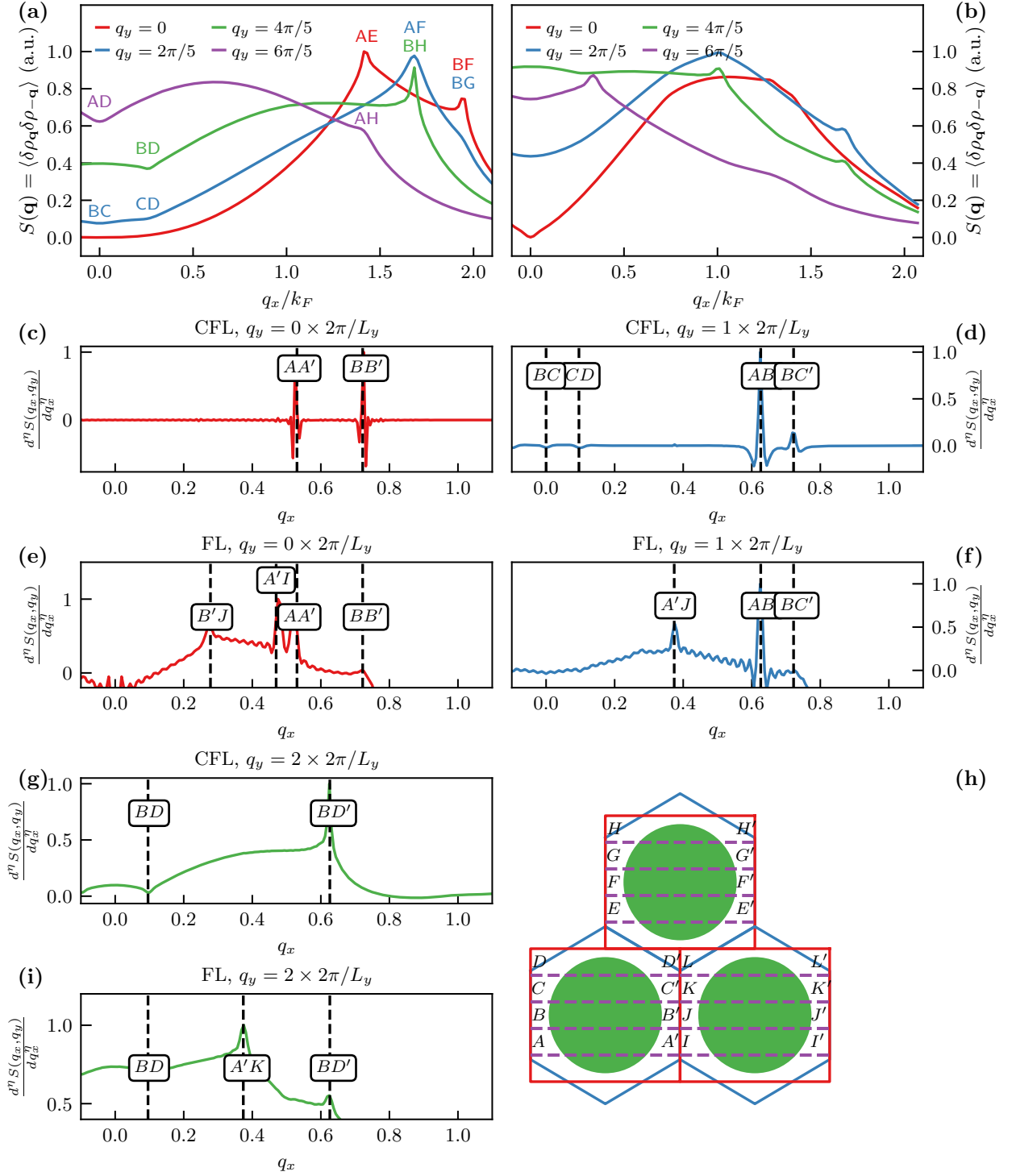


FIG. 12. Quantitative comparison between FL and CFL structure factors with Fermi surface scattering momenta. (a) Connected structure factor $S(\mathbf{q})$ at constant q_y as a function of q_x for the CFL phase (also shown in main text). (b) Same for the FL at $\epsilon_r = 60$. Fractional derivatives of $S(\mathbf{q})$ with respect to q_x to bring out detailed features are shown for $q_y = 0$ (c,e), $q_y = 1$ (d,f), and $q_y = 2$ (g,i). Note that some peaks are only clearly visible for FL or CFL. In particular, *umklapp* peaks between the first and higher Brillouin zones only clearly appear for the FL state. (h) Brillouin zone geometry and labelling scheme for vertical dashed lines. For instance, a line denoted ‘BD’ corresponds to the q_x position of $\mathbf{q} = \mathbf{k}_D - \mathbf{k}_B$, where \mathbf{k}_B and \mathbf{k}_D are intersections between the wires and the Fermi surface.

current in two setups. Using scanning tunneling microscope (STM), electrons can be directly injected into the sample. Alternatively, the tunneling current between two CFLs separated by a tunneling barrier can be measured. The contrast in zero bias features have been shown directly in Ref. [5], in which the second setup is employed in the Landau level setting.

Transport measurements give distinct signatures for the CFL. If we denote $\tilde{\rho}$ the (dimensionless) resistivity tensor for the CFL itself, in the half filled Landau level setting, the physical conductivity is given by:

$$\sigma = \frac{e^2}{2h} \left(\epsilon + \frac{\tilde{\rho}}{2} \right) \quad (\text{E1})$$

, where ϵ is the antisymmetric 2×2 tensor. Now, in the absence of disorder and of scattering of the composite fermions, $\tilde{\rho} \rightarrow 0$, which implies the longitudinal conductivity σ_{xx} vanishes. In contrast, in a clean Fermi liquid in a Chern band, the longitudinal conductivity is expected to *grow* as disorder is reduced [101]. One may further seek to measure thermoelectric transport signatures, encapsulated in the tensor $\mathbf{E} = \hat{S} \nabla \mathbf{T}$, where for the CFL in the half filled LL, $\hat{S} = \sigma^{-1} \epsilon \tilde{\rho} \tilde{\alpha} / 2$, where $\tilde{\alpha}$ is the thermoelectric conductivity of the composite Fermi surface Ref. [102, 103]. Finally, thermal conductivity measurements, although challenging, will serve as a smoking gun signature of the nFL, since the CFL will strongly violate the Wiedemann-Franz law [98]. Away from the CFL filling, the composite fermions experience an effective magnetic field tied to the filling deviation: $\Delta\nu = \nu - 1/2$, lead-

ing to Landau levels of the composite Fermi surface. FCIs correspond to fully occupying these Landau levels [1, 3], corresponding to fillings $\nu = -(p+1)/(2p+1)$, and the many-body gap of the FCI is identified with the cyclotron gap of the Landau levels. The observation of FCIs at filling $\nu = -2/3, -3/5$ in moiré TMDs [26, 27], corresponding to $p = 1, 2$ is consistent with this expectation. On the other hand, an FL would not exhibit such quantum oscillations when the filling is changed. Analogously, imposing a one-dimensional periodic grating is expected to lead to geometric resonances on varying the filling $\Delta\nu$ in the moiré TMD setting, as have been observed for CFLs in Landau levels [3, 6, 7].

A notable prediction of the CFL picture [3], verified in experiments [8] in the Landau level context, relates to the finite wave-vector conductivity $\sigma_{xx}(\mathbf{q})$ which can be probed by surface acoustic waves (SAWs). The CFL conductivity is predicted to be *linear* in the wave-vector $|\mathbf{q}|$. This follows directly from the form of the CFL conductivity tensor E1 combined with the fact that the intrinsic resistivity of the CFL in the clean limit is set by the finite wave-vector of the SAW probe $\tilde{\rho} \propto |\mathbf{q}|$.

Implementing the proposals above will require overcoming significant experimental challenges - from performing transport measurements on TMD moiré materials to working with the smaller size of moiré samples compared to GaAs/GaAlAs samples. Nevertheless, given the experimental opportunity to study a zero field non-Fermi liquid which is the parent state of a non-Abelian topological phase, we anticipate there will be strong push to tackle these challenges.